

# The Properties of the Progenitor Supernova, Pulsar Wind, and Neutron Star inside PWN G54.1+0.3

Joseph D. Gelfand

NYU Abu Dhabi

PO Box 903, New York, NY, 10276

jg168@nyu.edu

<sup>1</sup>

Patrick O. Slane

Harvard-Smithsonian Center for Astrophysics

60 Garden Street, Cambridge, MA 02138

and

Tea Temim

Observational Cosmology Lab, Code 665

NASA Goddard Space Flight Center

Greenbelt, MD 20771, USA

<sup>2</sup>

Received \_\_\_\_\_; accepted \_\_\_\_\_

---

ce, New York, NY 10003

and

<sup>2</sup>Oak Ridge Associated Universities, Oak Ridge, TN 37831, USA

## ABSTRACT

The evolution of a pulsar wind nebula inside a supernova remnant is sensitive to properties of the central neutron star, pulsar wind, progenitor supernova, and surrounding interstellar medium both difficult to measure directly and critical for understanding how neutron stars form and interact with their surroundings. In this paper, we determine these properties for PWN G54.1+0.3 by fitting its observed dynamical and broadband spectral properties with a model for the dynamical and radiative evolution for the evolution a pulsar wind nebula inside a supernova remnant. Our modeling suggests that the progenitor of G54.1+0.3 was a  $\sim 15 - 20 M_{\odot}$  which exploded inside a massive star cluster, creating a neutron star with an initial spin period  $P_0 \sim 30 - 80$  ms. When the pulsar wind is injected into the pulsar wind nebula at the termination shock,  $\gtrsim 99\%$  of the energy is in the kinetic energy of its component electrons and positrons, and the energy spectrum of these particles is well characterized by a broken power-law – somewhat consistent with the predictions of the latest numerical simulations. Lastly, we propose future observations which can both test the validity of this model and better determine the properties of this source.

*Subject headings:* pulsars: individual: PSR J1930+1852, ISM: individual objects: PWN G54.1+0.3, ISM: supernova remnants, X-rays: individual: PWN G54.1+0.3

## 1. Introduction

Stars born with a mass  $\gtrsim 8 M_{\odot}$  (Heger et al. 2003) are believed to end their lives in a core-collapse supernova which are powered by the gravitational collapse of the central Iron core into a neutron star (e.g. Zwicky 1938). In many cases, the collapse of the core creates a rapidly spinning (initial rotational period  $P_0 \ll 1$  s) neutron star with a strong ( $B \sim 10^{12}$  G) surface magnetic field often observed as a pulsar. Such neutron stars are spinning sufficiently rapidly to generate a flow of highly relativistic particles, most likely predominantly electrons and positrons, from the neutron star surface called a pulsar wind which decreases the rotational energy of the neutron star, causing the observed rotation period to increase (Goldreich & Julian 1969; Arons 2002).

Additionally, a small fraction of the gravitational energy released during the collapse is deposited in the star’s outer envelope, ejecting this material into the surrounding interstellar medium (ISM), creating a supernova remnant (SNR). Initially, the pulsar wind is injected into the SNR, and its confinement by the surrounding ejecta creates a “termination shock” where the pulsar wind is decelerated by the surrounding medium (Kennel & Coroniti 1984b; see Gaensler & Slane 2006 for a recent review). The expansion of the post-shocked (“downstream”) pulsar wind creates a PWN, whose evolution is sensitive to the properties of the central neutron star, the acceleration mechanism at the termination shock, and the surrounding medium, including the initial spin period  $P_0$  of the central neutron star and the mass and initial kinetic energy of the material ejected in the progenitor supernova (Kennel & Coroniti 1984a, Gelfand et al. 2009 and references therein).

However, determining these properties requires modeling the dynamical and radiative evolution of a PWN inside a SNR (e.g. Reynolds & Chevalier 1984; Gelfand et al. 2009; Tanaka & Takahara 2010; Bucciantini et al. 2011, again see Gaensler & Slane 2006 for a recent review). Such models have been developed, incorporating the effect of the spin-down

of the central neutron star (e.g. Bucciantini et al. 2004; Gelfand et al. 2009), properties of the progenitor supernova and surrounding ISM (e.g. Chevalier 2005; Gelfand et al. 2009), and the spectrum of particles injected into the PWN at the termination shock (Volpi et al. 2008; Fang & Zhang 2010; Bucciantini et al. 2011), on the observed properties of the PWN.

In this paper, we use a model for the radiative and dynamical evolution of a PWN inside a SNR to derive the physical characteristics of the neutron star, pulsar wind, progenitor supernova, and surrounding ISM for PWN G54.1+0.3. We describe this model in §2, and present the observed properties we aim to reproduce in §3.1. As described in this section, the detection of both a SNR around this PWN (Bocchino et al. 2010; Lang et al. 2010) and a radio pulsar PSR J1930+1852 at its center (Camilo et al. 2002; Lu et al. 2007) makes this system especially well-suited for this type of analysis. In §3.2 we describe the Markoff Chain Monte Carlo routine used to fit this data. This allowed us to explore the entire possible parameter space for the various unknown quantities, instead of simply finding a single set of parameters that reproduce the observed properties of a given PWN (e.g. Gelfand et al. 2007). We then compare our results to past analyses of this system (§3.2.1). In §4, we discuss the implications of these results concerning the progenitor of this system (§4.1), the formation of its associated pulsar (PSR J1930+1852; §4.2), and both the production and acceleration of particles in the pulsar wind (§4.3). Finally, in §5, we predict the results of potential observations of this source with new observing facilities, e.g., *NuStar* and LOFAR, and discuss the possible implications of these results. Lastly, in §6, we summarize our results and discuss its implications.

## 2. Evolutionary Model

Our model for dynamical and radiative evolution of a PWN inside a SNR is based on that of Gelfand et al. (2009). We assume the rotational luminosity  $\dot{E}$  of the central neutron

star evolves as (e.g. Gaensler & Slane 2006):

$$\dot{E}(t) = \dot{E}_0 \left( \frac{1}{1 + \frac{t}{\tau_{\text{sd}}}} \right)^{-\frac{p+1}{p-1}}, \quad (1)$$

where  $t$  is the time since the progenitor supernova,  $\dot{E}_0$  is the neutron star’s initial spin-down luminosity,  $\tau_{\text{sd}}$  is neutron star’s “spin-down” timescale, and  $p$  is the neutron star’s braking index (Gelfand et al. 2009), and that all of the rotational energy of the neutron star is carried away by the pulsar wind generated in its magnetosphere.

As discussed in §1, the pulsar wind is injected into the PWN at the termination shock, and both the evolution and emission of PWN depends on the magnetization and spectrum of particles at injection. We assume that a constant fraction  $\eta_B$  of the energy injected at the termination shock is in the form of magnetic fields, while the rest  $1 - \eta_B$  in the kinetic energy of electrons and positrons (Gelfand et al. 2009). Theoretical studies predict that, under most physical conditions, the spectrum of injected particles is well described by a relativistic Maxwellian with a high-energy power-law tail (e.g. Spitkovsky 2008; Sironi & Spitkovsky 2011). While this spectrum can reproduce the broadband spectral energy distribution (SED) of some PWNe (e.g., Fang & Zhang 2010), we find it doesn’t work for G54.1+0.3 for constant parameters. However, our model can reproduce the observed SED if the spectrum of these particles is well described by a broken power-law:

$$n(E) = \begin{cases} n_{\text{break}} \left( \frac{E}{E_{\text{break}}} \right)^{-p_1} & E_{\text{min}} < E < E_{\text{break}} \\ n_{\text{break}} \left( \frac{E}{E_{\text{break}}} \right)^{-p_2} & E_{\text{break}} < E < E_{\text{max}} \end{cases}, \quad (2)$$

where  $E_{\text{min}}$  is the minimum energy particle injected into the PWN,  $E_{\text{break}}$  is the break energy in the spectrum,  $E_{\text{max}}$  is the maximum energy particle injected into the PWN, and  $n(E)\Delta E \Delta t$  is the number of electrons and positrons injected in the PWN between energies  $E$  and  $E + \Delta E$  in time  $\delta t$ , and  $n_{\text{break}} \equiv n(E_{\text{break}})$ . We calculate  $n_{\text{break}}(t)$  by requiring the

energy injection rate of relativistic particles into the PWN is  $(1 - \eta_B)\dot{E}$ , or:

$$(1 - \eta_B)\dot{E} = \int_{E_{\min}}^{E_{\max}} En(E)dE. \quad (3)$$

Recent simulations (e.g., Sironi & Spitkovsky 2011; Sironi et al. 2013) have been able to produce this injection spectrum under certain situations, and this spectral shape has been used to reproduce the broadband SED of this PWN and others in similar work (e.g. Chevalier 2005; Bucciantini et al. 2011).

As in Gelfand et al. (2009), the dynamical evolution of the PWN is calculated by assuming the difference in pressure inside the PWN and inside the SNR just outside the PWN results in a net force on the shell of swept-up material surrounding the PWN. The pressure inside the PWN depends significantly on both the adiabatic and radiative losses (assumed to be dominated by synchrotron emission and inverse Compton scattering off Cosmic Microwave Background photons) of the electrons and positrons inside the PWN. Similarly to Gelfand et al. (2009), we use a “one-zone” model for the PWN – assuming that both the PWN’s magnetic field strength  $B_{\text{pwn}}$  and the particle density are constant. We then calculate the resultant photon spectrum using the same procedure described in Gelfand et al. (2009). This model assumes that particles do not escape the PWN, though recent works suggests this not a dominant factor for young PWN like G54.1+0.3 (e.g., Martin et al. 2012).

### 3. Observed and Fitted Properties

In this section, we first (§3.1) present the observed properties of G54.1+0.3 we wish to reproduce, and then (§3.2) describe the algorithm used to fit the data with our model, the best-fit parameters, and discuss the degeneracies between parameters. Finally, we compare our results with similar work (§3.2.1).

### 3.1. Observed Properties

As mentioned in §1, G54.1+0.3 is one of the best studied PWN. Both pulsed radio (Camilo et al. 2002) and X-ray (Lu et al. 2007) emission are detected from the central neutron star, PSR J1930+1852, and the measured period  $P$  and period-derivative  $\dot{P}$  provide estimates for its current spin-down luminosity  $\dot{E}$ , characteristic age  $t_{\text{ch}}$ , and strength of the dipole component to its surface magnetic field. Since the errors on  $\dot{E}$  and  $t_{\text{ch}}$  are small (Camilo et al. 2002), we use their measured values (Table 1) to determine the initial spin-down luminosity  $\dot{E}_0$  and true age  $t_{\text{age}}$  for each trial combination of the model parameters (§3.2).

This PWN has also been detected across the electromagnetic spectrum. Since the radio emitting particles are among the oldest in the PWN (e.g., Gelfand et al. 2009), we use the radio extent to determine its angular size – though its radio and X-ray extent are similar (e.g., Lu et al. 2001; Lang et al. 2010; Temim et al. 2010). This PWN is considerably elongated at both radio energies (Lang et al. 2010), with a semi-major axis of  $\sim 1.25'$  and a semi-minor axis of  $\sim 1.0'$  (Lang et al. 2010). Since our model assumes a spherically symmetric PWN (§2), we require our model reproduce the “average” of its measured semi-minor and semi-major axes  $\theta_{\text{pwn}}$ , and use these to determine the  $3\sigma$  lower and upper limits on  $\theta_{\text{pwn}}$ , respectively (Table 1). While we do not fit the angular radius of the termination shock estimated from *Chandra* observations of this PWN (semi-major axis  $\theta_{\text{ts}} \approx 5.7''$ , Lu et al. 2001; Temim et al. 2010), we use this value in the theoretical interpretations presented in §4.3.

We also require our model to reproduce the observed radio (Lang et al. 2010), X-ray (Temim et al. 2010), and TeV  $\gamma$ -ray spectrum (Acciari et al. 2010), since emission in these wavebands is likely dominated by particles inside the PWN (Table 1). This contrasts with its mid-infrared (mid-IR) emission (Koo et al. 2008; Temim et al. 2010), which appears to

result from material shocked and heated by the expanding PWN. Because we are using a one-zone model (§2), we do not attempt reproduce spatial variations in its X-ray spectrum (e.g., Temim et al. 2010; Lu et al. 2001), but fit its global X-ray properties (excluding emission from the pulsar), specifically the 2-10 keV unabsorbed X-ray flux  $F_{\text{X},2-10}$  and photon index  $\Gamma$  (Table 1) obtained when fitting the observed emission with an absorbed power-law (Temim et al. 2010).

Our model must also reproduce the observed properties of the SNR. Since our model does not simulate emission from the SNR itself, we only attempt to reproduce its angular size. The SNR around PWN G54.1+0.3 has been detected at both radio (Lang et al. 2010) and X-ray (Bocchino et al. 2010) energies, each reporting a somewhat different angular radius  $\theta_{\text{snr}}$ . To resolve this discrepancy, we analyzed an archival D-array 1.4 GHz VLA observation of this PWN, estimating a SNR angular radius of  $\approx 6'.6$ . We then estimated the error on  $\theta_{\text{snr}}$  by setting  $3\sigma$  upper and lower limits to those reported by Lang et al. (2010) and Bocchino et al. (2010) .

Lastly, we need to assume a distance to convert the physical properties returned by our evolutionary model (§2) into the observed quantities described above. Analysis of the H $\alpha$  absorption spectrum measured towards this PWN suggest that G54.1+0.3 is between 4.5 – 9 kpc away (Leahy et al. 2008), we prefer distances between these values in the fitting algorithm described in §3.2.

### 3.2. Model Fit

In order to derive the physical properties of the central neutron star, pulsar wind, and progenitor supernova of G54.1+0.3, we need to fit its observed properties (Table 1; §3.1) using the physical parameters (Table 2) of our evolutionary model (§2). This is simplified by

the measured characteristic age  $t_{\text{ch}}$  and current spin-down luminosity  $\dot{E}$  of PSR J1930+1852 (Camilo et al. 2002), which allows us to set the true age  $t_{\text{age}}$  of G54.1+0.3 to:

$$t_{\text{age}} = \frac{2\tau_{\text{ch}}}{p-1} - \tau_{\text{sd}}, \quad (4)$$

and the initial spin-down luminosity  $\dot{E}_0$  of this pulsar to:

$$\dot{E}_0 = \dot{E} \left( 1 + \frac{t_{\text{age}}}{\tau_{\text{sd}}} \right)^{\frac{p+1}{p-1}}. \quad (5)$$

ensuring each trial reproduces the observed properties of this pulsar.

We use a Metropolis Markoff Chain Monte Carlo (MCMC) algorithm to determine which combination of the 12 model parameters  $\theta$  best reproduce the 12 observed properties  $\mathcal{D}$  listed in Table 1. For a given combination, we calculate the expected value of each observed properties  $\mathcal{M}$ . We then define the likelihood  $\mathcal{L}(\mathcal{D}|\theta)$  that this set of parameters accurately represents the data using the following formula:

$$\mathcal{L}(\mathcal{D}|\theta) = \prod_{i=1}^{12} \frac{1}{\sqrt{2\pi}\sigma_i} e^{-\frac{1}{2} \left( \frac{\mathcal{M}_i - \mathcal{D}_i}{\sigma_i} \right)^2}, \quad (6)$$

where  $\sigma_i$  is the error on each observed quantity. This expression implicitly assumes that the error on each observable is Gaussian in nature. The MCMC algorithm searches the parameter space to find the combinations that maximize  $\ln \mathcal{L}$ :

$$\ln \mathcal{L} = -\frac{1}{2} \sum_{i=1}^{12} \ln \left( \frac{1}{\sqrt{2\pi}\sigma_i} \right) \times \left( \frac{\mathcal{M}_i - \mathcal{D}_i}{\sigma_i} \right)^2 \quad (7)$$

$$\propto -\chi^2, \quad (8)$$

where  $\chi^2$  is defined as:

$$\chi^2 = \sum_{i=1}^{12} \left( \frac{\mathcal{M}_i - \mathcal{D}_i}{\sigma_i} \right)^2. \quad (9)$$

Therefore maximizing  $\ln \mathcal{L}$  is equivalent to minimizing  $\chi^2$ .

This algorithm samples the parameters space using the following procedure:

1. For a given combination  $\theta_n$ , evaluate  $\ln \mathcal{L}_n$ .
2. Propose  $\theta_{n+1}$  which is  $\theta_n + f(\theta)$ , where  $f(\theta)$  is a set of random, zero-mean, Gaussian distributed numbers whose width varies for each model parameter.
3. Calculate  $\ln \mathcal{L}_{n+1}$  for the proposed  $\theta_{n+1}$ .
4. If  $\ln \mathcal{L}_{n+1} \geq \ln \mathcal{L}_n - \delta$ , where  $\delta$  is a random number, then  $\theta_{n+2}$  is calculated with  $\theta_{n+1}$  as a starting point. Otherwise,  $\theta_{n+2}$  is calculated with  $\theta_n$  as a starting point.

The average size of the random adjustments to the parameters done in Step 2 were chosen such that the  $\theta_{n+1}$  satisfies the above condition 25% – 40% of the time (Mandel, private communication). To make sure we probe the entire parameter space, we conducted 45 MCMC runs with different initial parameters, each with 50000 trials. These initial values were concentrated in regions favored by our current theoretical ( $E_{\text{sn}} \sim 10^{51}$  ergs and  $M_{\text{ej}} \lesssim 20 \text{ M}_\odot$ ; Heger et al. 2003) and observational ( $p \lesssim 3$ ; Livingstone 2011) understanding of these sources. The set of parameters with the lowest  $\chi^2$  (Table 3) is able to reproduce both the dynamical and radiative properties of this source (Table 3, Figure 1).

Not surprising, there are significant degeneracies between different model parameters. For example, the initial kinetic energy  $E_{\text{sn}}$  and mass  $M_{\text{ej}}$  of the supernova ejecta are degenerate with each other and the density of the surrounding ISM (Figure 2) – similar to what was found in a similar analysis of Kes 75 (Gelfand et al. 2014). As a result, our model can reproduce the observed properties of G54.1+0.3 with ejecta masses significantly lower than the best fit  $M_{\text{ej}} \approx 22 \text{ M}_\odot$ , albeit for low energy explosions ( $E_{\text{sn}} < 10^{51}$  ergs) occurring in a low density ( $n_{\text{ism}} < 10^{-3} \text{ cm}^{-3}$ ) environment. The braking index  $p$  and spin-down timescale  $\tau_{\text{sd}}$  are degenerate with each other and both the initial spin period  $P_0$  and true age  $t_{\text{age}}$  of PSR J1930+1852 (Figure 3) – the latter two a direct result of its period  $P$  and characteristic age  $t_{\text{ch}}$  (Table 1; Camilo et al. 2002), with the age  $t_{\text{age}}$  also being degenerate

with the distance (Figure 4). Additionally, the distance  $d$  as well as the break energy  $E_{\text{break}}$  and high-energy particle index  $p_2$  in the injection spectrum are all degenerate with the magnetization of the pulsar wind  $\eta_B$  (Figure 5). Lastly, the particle index below the break energy  $p_1$  is degenerate with the break energy (Figure 6), with higher values of the break energy requiring a softer injection spectrum.

Thanks to our search of parameter space, we can determine the 90% confidence interval (Table 4) of a given parameter by the 5th and 95th percentile values in the combined list of accepted trials from all the MCMC chains (Hogg, private communication). However, since the trial values are biased by the choice of initial parameters for the various MCMC chains, this can result in the parameter value for the trial with the lowest  $\chi^2$  falling outside its nominal 90% confidence interval. For examples, we initialized all our MCMC chains with  $p < 3$  as observed (e.g., Livingstone 2011), even though the trial with the lowest  $\chi^2$  had a braking index  $p \approx 3$  (Table 3). This explains why the “best” value of  $p$  is not within the quoted 90% confidence interval (Table 4). Because  $p$  and  $\tau_{\text{sd}}$  are degenerate with each other (Figure 3), the “best” value of  $\tau_{\text{sd}}$  also falls outside the 90% confidence interval of this parameter (Table 4).

### 3.2.1. Comparison with other models

In this section, we compare the results of our analysis of G54.1+0.3 with that done by other models. Chevalier (2005) uses the measured spectral properties and radius of this PWN and the spin-down properties of the central pulsar to primarily estimate the birth properties of the neutron star. It does not attempt to reproduce the broadband spectral energy distribution (SED), and sets  $p_1$  and  $p_2$  to values inferred from single power-law fits to the observed radio and X-ray spectrum (Chevalier 2005). While the value of  $p_2$  derived from this method agrees with our value, the value of  $p_1$  does not since the SED predicted by

our model contains a spectral break between 1.4 and 4.8 GHz (Figure 1). Additionally, this analysis assumes that  $\eta_B = \frac{3}{7}$  (Chevalier 2005), a significantly higher value than allowed by our fits. As a result, in it favors a lower total particle energy inside this PWN then our model, resulting in a significantly higher initial period  $P_0$ . Lastly, this analysis assumes  $M_{ej} \equiv 5 M_\odot$  and  $E_{sn} = 10^{51}$  ergs, a combination not favored by our fits (Figure 2).

The analysis of Bocchino et al. (2010) infer the age and the properties of both the progenitor supernova and surrounding ISM from the X-ray emission associated with the SNR shell. Since they did not attempt to reproduce the broadband SED of this source, this analysis does not constrain the magnetization or spectrum of particles injected into the PWN at the termination shock. They derive  $n_{ism} \sim 0.2 \text{ cm}^{-3}$  assuming a distance of  $d \equiv 6.2 \text{ kpc}$  and primarily thermal X-ray emission, higher than the values preferred by our modeling (Table 4). The age  $t_{age}$  and supernova explosion energy  $E_{sn}$  they derive are sensitive to ratio of the electron and ion temperatures, with  $E_{sn} = (0.3 - 0.7) \times 10^{51}$  ergs and  $t_{age} \sim 2500 - 3300$  years if the electrons and ions are in equipartition, while  $E_{sn} = (0.5 - 1.6) \times 10^{51}$  ergs and  $t_{age} \sim 1800 - 2400$  years if the ions are  $\sim 2\times$  hotter than the electrons. Both sets of  $E_{sn}$  and  $t_{age}$  are consistent with our results (Table 4). The authors also found that the radius of the PWN and SNR are consistent with  $M_{ej} = 8 M_\odot$ ,  $p = 3$ , and  $\tau_{sd} = 500$  years (Bocchino et al. 2010) – in agreement with our results.

G54.1+0.3 was also analyzed by Tanaka & Takahara (2011), who attempt to reproduce both the size and broadband SED of this PWN using a model very similar to ours (§2). The most significant between their analysis and ours is they consider inverse Compton scattering of electrons off photon fields other than the CMB: an optical ( $T = 4000 \text{ K}$ ) photon field with an energy density  $u_{opt} = 0.5 \text{ eV cm}^{-3}$ , and a IR ( $T = 40 \text{ K}$ ) photon field with having an energy density  $u_{ir} = 0.5 \text{ eV cm}^{-3}$  or  $u_{ir} = 2.0 \text{ eV cm}^{-3}$  (Tanaka & Takahara 2011). These authors found that  $\eta_B$ ,  $E_{break}$ , and the parameters associated with the energetics of

the neutron star ( $\tau_{\text{sd}}$ ,  $t_{\text{age}}$ ,  $\dot{E}_0$ , and  $P_0$ ) depended on  $u_{\text{ir}}$  (Table 4; Tanaka & Takahara 2011). While they found a similar value of  $\tau_{\text{sd}}$  when  $p \approx 3$  ( $\tau_{\text{sd}} \sim 100 - 1000$  years; Figure 3), this model favors a less energetic neutron star due to these additional photon fields.

Similar results we obtained by Torres et al. (2014), who use the evolutionary model of Martin et al. (2012) that includes the diffusion of particles both inside and out of the PWN, to model the size and broadband SED of this system. Like Tanaka & Takahara (2011), they include emission from electrons inverse Compton scattering off two photon fields in addition to the CMB, one with  $T_{\text{FIR}} = 20$  K and energy density  $u_{\text{FIR}} = 2.0 \text{ eV cm}^{-3}$  and the other with  $T_{\text{NIR}} = 3000$  K and energy density  $u_{\text{FIR}} = 1.1 \text{ eV cm}^{-3}$  (Torres et al. 2014). As a result, they derive a lower  $\dot{E}_0$  (higher  $P_0$ ) than our analysis. This can also explain why the spin-down timescale  $\tau_{\text{sd}}$  is higher than that favored by our model for  $p = 3$ . This model assumes the maximum energy of particles is variable, and limited by confinement in the termination shock, though the current value they predict is similar to what we require for our model.

Lastly, we compare our results with that of Li et al. (2010), which model the broadband SED of G54.1+0.3 for both a leptonic and combined leptonic and hadronic origin for the observed  $\gamma$ -rays. Like Torres et al. (2014), the maximum energy of particles injected at the termination shock  $E_{\text{max}}$  varies, though in this case is set to energy whose Larmor radius is the radius of the PWN (Li et al. 2010). Their model assumes that Bohm diffusion is responsible for leptons escaping from the PWN, and these particles inverse Compton scatter off background IR and optical photons from the Milky Way, emission from the IR “loop” and its embedded point sources around this PWN (Koo et al. 2008; Temim et al. 2010), in addition to the CMB. In the purely leptonic case, Li et al. (2010) derive similar values of  $\eta_B$  and  $p_2$  despite assuming very different values of  $E_{\text{min}}$ ,  $E_{\text{break}}$ , and  $p_1$  (Table 4). They further argue that, since this scenario favors a PWN magnetic field strength

( $B_{\text{pwn}} \sim 10\mu\text{G}$ ) significantly weaker than the strength ( $\sim 40 - 200\mu\text{G}$ ) inferred from the radio luminosity and polarization (Lang et al. 2010), that  $\sim 87\%$  of the spin-down luminosity of this pulsar is injected into this PWN in the form of ions (Li et al. 2010).

#### 4. Fit Implications

As described in §1, the derived properties of the supernova ejecta, surrounding ISM, pulsar, and pulsar wind presented in §3.2 allow us to estimate the properties of the stellar progenitor (§4.1) and the birth properties of the central pulsar (§4.2), and provide insight to the generation and acceleration of particles in the pulsar wind (§4.3).

##### 4.1. Progenitor Star

The initial kinetic energy  $E_{\text{sn}}$  and mass  $M_{\text{ej}}$  ejected in a core-collapse supernova depends on the initial mass, metallicity, and evolution of the progenitor star (e.g., Heger et al. 2003). G54.1+0.3 has a galactocentric radius ( $\sim 6.5 - 7.5$  kpc for the favored distance of  $d \sim 5 - 8$  kpc) similar to the Sun’s ( $\sim 8 - 8.5$  kpc; Andrievsky et al. 2002a,b), suggests the progenitor star had approximately Solar metallicity. As discussed in §3.2, our model suggests that – even for low energy explosions – the progenitor supernova ejected  $\gtrsim 3 M_{\odot}$  of material (Figure 2). This suggests the progenitor did not have a binary companion, since the mass transfer expected to occur during a binary’s evolution is expected to result in a very low ejecta mass (e.g.,  $\lesssim 3 M_{\odot}$ ; e.g., Woosley et al. 2002).

Therefore, we assume that the progenitor of this system was an isolated massive star. Such stars are believed to produce a neutron star when they (e.g., Woosley et al. 2002):

- have an initial mass of  $\sim 8 - 20 M_{\odot}$ , in which case they explode as a red supergiant

(most likely producing a Type IIp supernova), ejecting a lot of material ( $\gtrsim 6 - 15 M_{\odot}$ ), or

- having extremely high ( $\sim 50 M_{\odot}$ ) initial mass but explodes after shedding much of this mass as a Wolf-Rayet star (most likely producing a Type Ib/c supernova), resulting in a low ( $\lesssim 3 M_{\odot}$ ) ejecta mass.

While our model can reproduce the observed properties of G54.1+0.3 for both ranges of ejecta mass, our fitting suggests that a low ejecta mass ( $\sim 3 M_{\odot}$ ) requires a low energy ( $E_{\text{sn}} \lesssim 10^{50}$  ergs) supernova while a more “canonical” supernova explosion energy of  $E_{\text{sn}} \sim (0.3 - 1) \times 10^{51}$  ergs requires a higher ejecta mass ( $M_{\text{ej}} \gtrsim 10 M_{\odot}$ ; Figure 2).

Since our model requires the PWN has not yet collided with the SNR reverse shock (Figure 7), its dynamical evolution is very sensitive to the mass  $M_{\text{ej}}$  and initial kinetic energy  $E_{\text{sn}}$  of the progenitor explosion (Gelfand et al. 2009). We can constrain this evolution using the properties of the PWN inferred from analysis of the surrounding IR shell (Koo et al. 2008; Temim et al. 2010). A spectral analysis of this emission suggests it is composed primarily of supernova ejecta, consistent with the PWN not having yet collided with the reverse shock (Figure 7). This shell contains  $\sim 0.05 M_{\odot}$  of dust (Temim et al. 2010) which, since  $\lesssim 5\%$  of the supernova ejecta is expected to condense into dust grains (Kozasa et al. 2009), requires the PWN has swept up  $\gtrsim 1 M_{\odot}$  of ejecta. This criterion is satisfied for trials where the supernova ejected  $\gtrsim 10 M_{\odot}$  of material with a “normal” ( $\gtrsim 0.3 \times 10^{51}$  ergs) initial kinetic energy but not for those with both a low ejecta mass ( $\lesssim 3 M_{\odot}$ ) and initial kinetic energy ( $\lesssim 10^{50}$  ergs; Figure 8). Therefore, our model favors a  $\sim 15 - 20 M_{\odot}$  progenitor.

This is further supported by the  $\gtrsim 500 \text{ km s}^{-1}$  expansion velocity of the IR shell inferred from the width of molecular lines, which is consistent with the values of  $v_{\text{pwn}}$  predicted by our model (Figure 8). This material in the bright IR knot detected in this region is also believed to be heated by a  $\sim 25 \text{ km s}^{-1}$  shock (Temim et al. 2010), likely

driven by the expanding PWN. For different trials, we can estimate the speed of the shock driven into the ejecta by the expanding PWN,  $v_{\text{pwn,shock}}$  as:

$$v_{\text{pwn,shock}} \approx v_{\text{pwn}} - v_{\text{ej}}(R_{\text{pwn}}), \quad (10)$$

where  $v_{\text{ej}}(R_{\text{pwn}})$  is the expansion velocity of the ejecta just outside the PWN. While our model predicts that  $v_{\text{pwn,shock}} \sim 50 - 150 \text{ km s}^{-1}$  (Figure 8), somewhat higher than the shock speed inferred from the spectrum of the IR knot, this can be attributed to the higher than average density in this region (Temim et al. 2010) which would result in a slower shock. Since lower values of  $v_{\text{pwn,shock}}$  favor a larger ejecta mass (Figure 8), this again favors a  $\sim 15 - 20 M_{\odot}$  progenitor. Furthermore, the identification of O and B stars embedded inside the SN ejecta dust surrounding this PWN (Temim et al. 2010) suggests the progenitor was the first star in this cluster to explode, and therefore was its most massive member – again, consistent with a  $\sim 15 - 20 M_{\odot}$  progenitor.

This progenitor mass, and association with an massive star cluster, can explain the low ISM density required by our model (Table 4). The main-sequence winds of massive stars are thought to create low-density bubble with a radius  $R_b$  (Chen et al. 2013):

$$R_b = \left[ (1.22 \pm 0.04) \frac{M}{M_{\odot}} - (9.16 \pm 1.77) \right] \left( \frac{P_{\text{ism}}/k_B}{10^5 \text{ cm}^{-3} \text{ K}} \right)^{-\frac{1}{3}} \text{ pc} \quad (11)$$

$$\sim 7 - 18 \left( \frac{P_{\text{ism}}/k_B}{10^5 \text{ cm}^{-3} \text{ K}} \right)^{-\frac{1}{3}} \text{ pc}, \quad (12)$$

where  $P_{\text{ism}}$  is the pressure of the medium outside the wind bubble and  $k_B$  is Boltzmann's constant. For a distance of  $\sim 4.5 - 9 \text{ kpc}$  (Leahy et al. 2008), this translates to an angular size of  $\theta_b \sim 2'7 - 14'$ . Winds from the additional massive stars in the cluster will only cause increase the size of this bubble, increasing the likelihood that the SNR is expanding inside a stellar wind bubble.

## 4.2. Neutron Star Formation and Evolution

The birth properties of a neutron star reflect the physics of its formation. The initial spin period  $P_0$  and surface magnetic field of the neutron star depend on the properties of its progenitor, particularly the rotation rate of its iron core (e.g., Ott et al. 2006), and instabilities active during the supernova explosion itself (e.g., Blondin & Mezzacappa 2007; Endeve et al. 2010), while the spin-down evolution of the neutron star (e.g., its braking index  $p$  and spin-down timescale  $\tau_{\text{sd}}$ ) is likely to depend on its internal structure (e.g., Ho & Andersson 2012). While the theory connecting these parameters to the underlying physics is far from settled, measuring these quantities provides important information on these processes. For example, if the initial spin period of the neutron star is determined by the “fallback” of material during the supernova and resultant  $r$ -mode instabilities in the proto-neutron star, an initial spin period of  $P_0 \sim 30 - 80$  ms (Watts & Andersson 2002) is required to explain the  $\sim 10^{13}$  G dipole surface magnetic field strength inferred from the timing properties of PSR J1930+1852 (Camilo et al. 2002) – remarkably similar to the range favored by our model (Table 4).

## 4.3. Pulsar Wind

The pulsar wind is believed to be powered by the rotational energy of the neutron star which, due to the electric potential (voltage) generated at the magnetic poles  $\Phi$ :

$$\Phi = \sqrt{\frac{\dot{E}}{c}}, \quad (13)$$

leads to the creation of particles in the magnetosphere (e.g., Goldreich & Julian 1969). This potential is expected accelerate electrons and positrons to an energy of  $e\Phi$ , where  $e$  is the charge of the positron. Based on its current spin-down luminosity  $\dot{E}$  of (Table 1; Camilo et al. 2002), the magnetosphere of PSR J1930+1852 is capable of accelerating particles to

$\approx 6$  PeV, consistent with the range of  $E_{\max}$  suggested by our modeling (Table 4).

The pulsar wind consists of particles which exit the magnetosphere along open field lines, which is expected to occur at a minimum rate  $\dot{N}_{\text{GJ}}$  of (Goldreich & Julian 1969; Bucciantini et al. 2011):

$$\dot{N}_{\text{GJ}} = \frac{c\Phi}{e} = 7.6 \times 10^{33} \left( \frac{I_{45}}{P_{33}^3} \frac{\dot{P}}{4 \times 10^{-13} \text{ s/s}} \right)^{\frac{1}{2}} \text{ s}^{-1}, \quad (14)$$

where the neutron star's moment of inertia is  $I = I_{45} \times 10^{45}$  g cm<sup>2</sup>,  $P_{33} = P/33$  ms, and  $\dot{P}$  is the neutron star's period-derivative. Assuming that particles are neither created nor destroyed between the light cylinder and the termination shock, the rate  $\dot{N}$  at which particles leave the magnetosphere can be calculated using Equations 2 & 3 for a particular trial. Since we assume the parameters regulating the spectrum of particles injected at the termination shock ( $E_{\min}$ ,  $E_{\text{break}}$ ,  $E_{\max}$ ,  $p_1$ , and  $p_2$ ; Table 2) are constant,  $\dot{N} \propto \dot{E}$ . As result, the multiplicity of the pulsar wind  $\kappa$ :

$$\kappa \equiv \frac{\dot{N}}{\dot{N}_{\text{GJ}}}, \quad (15)$$

varies with time. Therefore, in addition to calculating the current multiplicity  $\kappa_{\text{now}}$ , we calculate the time-integrated multiplicity  $\kappa_{\text{int}}$ :

$$\kappa_{\text{int}} = \frac{\int_0^{t_{\text{age}}} \dot{N} dt}{\int_0^{t_{\text{age}}} \dot{N}_{\text{GJ}} dt}. \quad (16)$$

Our model requires that the current multiplicity  $\kappa_{\text{now}} \approx 10^3$  and the time-integrated multiplicity is  $\kappa_{\text{int}} \sim (1 - 3) \times 10^5$ , both in good agreement with the values derived from similar analyses of other PWNe (Figure 9; e.g., de Jager 2007). Since our model requires that  $p_1 > 0$  and  $p_2 > 0$  (Table 4), the multiplicity strongly depends on the minimum particle energy  $E_{\min}$  injected in the PWN at the termination shock (Figure 9). The small range of allowed  $\kappa$  and  $\kappa_{\text{int}}$  results from the  $E_{\min} \approx 10$  GeV required by our model (Figure

10). This tight constraint possibly results from fitting the apparent “break” in the radio spectrum observed around 4.8 GHz (§3.1; Table 3, Figure 1) with a model with an equal number of free parameters and data points (i.e., our fit has zero degrees of freedom). In §5, we suggest future observations which can test this result.

Near the neutron star, the pulsar wind is expected to be highly magnetized ( $\eta_B \approx 1$ ). However, our model requires that  $\eta_B \sim 10^{-3}$  (Table 4) when the pulsar wind is injected into the PWN – requiring that magnetic energy is converted to particle energy between the neutron star’s light cylinder and the termination shock (e.g., Kirk & Skjæraasen 2003). Currently, magnetic reconnection in this region is believed to transform the pulsar wind from a strongly magnetized to a weakly magnetized outflow (e.g., Kirk & Skjæraasen 2003; Sironi & Spitkovsky 2011, 2014). Efficient magnetic reconnection requires that (Equation 50 in Kirk & Skjæraasen 2003):

$$\mu < 3 \left( \frac{\pi^3 e^2}{m_e^2 c^5} \dot{E} \right)^{\frac{1}{4}} \quad (17)$$

where  $e$  and  $m_e$  are, respectively, the charge and mass of a positron,  $c$  is the speed of light, and  $\mu$  is the energy per unit mass energy of the pulsar wind (Equation 23 in Kirk & Skjæraasen 2003):

$$\mu \equiv \frac{\dot{E}}{\dot{N} m c^2}, \quad (18)$$

equivalent to the bulk Lorentz factor of the pulsar wind  $\gamma_w$  before it reaches (“upstream”) from the termination shock. For the values of  $\mu$  favored by our model ( $\mu \approx (1.5 - 2.5) \times 10^5$ ; Figure 11), magnetic reconnection is viable as long as the spin-down luminosity of PSR J1930+1852 is:

$$\dot{E} > \frac{m_e^2 c^5}{\mu} 81 \pi^3 e^2 \approx (0.2 - 1.3) \times 10^{35} \frac{\text{ergs}}{\text{s}}, \quad (19)$$

well below the  $\dot{E} \approx 10^{37} \frac{\text{ergs}}{\text{s}}$  suggested by its current spin-down properties (Table 1; e.g., Camilo et al. 2002). Therefore, we expect magnetic reconnection to occur upstream of the

termination shock, and is possibly responsible for the low wind magnetization required by our model.

However, the neutron star magnetosphere is not expected to result in particles whose spectrum is well-described by a broken power-law. Particle acceleration resulting from magnetic reconnection in the pulsar wind can produce particles whose spectrum is well-described by a power-law with particle index  $p \lesssim 2$  – as required by our modeling for  $E < E_{\text{break}}$  (Table 4) – if the ratio of magnetic to particle energy of the wind  $\sigma \gtrsim 10$  (Sironi & Spitkovsky 2014), where

$$\sigma = \frac{\eta_B}{1 - \eta_B}. \quad (20)$$

The maximum energy of particles expected to be accelerated in this scenario is (Sironi & Spitkovsky 2014):

$$E_{\text{max,recon}} \sim m_e c^2 \left[ \frac{(\sigma + 1)(2 - p)}{(p - 1)} \right]^{\frac{1}{2-p}}. \quad (21)$$

If magnetic reconnection is responsible for generating particles below the break, for a given trial we can estimate the magnetization of the reconnection layer  $\sigma_{\text{recon}}$  by equating  $p = p_1$  and  $E_{\text{max,recon}} = E_{\text{break}}$ :

$$\sigma_{\text{recon}} \sim \frac{p_1 - 1}{2 - p_1} \left( \frac{E_{\text{break}}}{m_e c^2} \right)^{2-p_1} - 1. \quad (22)$$

We find that  $\sigma_{\text{recon}} \gtrsim 10$  for the combinations of  $E_{\text{break}}$  and  $p_1$  preferred by modeling (Figure 12), suggesting that magnetic reconnection is a viable mechanism for producing the low-energy component of the injection spectrum.

Additional particle acceleration is expected to occur at the termination shock. Simulations suggest that efficient acceleration of an electron-positron plasma in this region requires  $\eta_B \lesssim 10^{-3}$  (e.g., Sironi et al. 2013), consistent with the range of values favored by our modeling for a lower distance ( $d \lesssim 6$  kpc), break energy ( $E_{\text{break}} \lesssim 30$  TeV), “harder”

low-energy particle spectrum ( $p_1 \lesssim 1.8$ ) but a “softer” high-energy particle spectrum ( $p_2 \gtrsim 2.7$ ; Figures 5 & 6). The maximum energy of particles produced in these shock is primarily limited by synchrotron cooling in the shock region,  $E_{\max,\text{synch}}$  (Sironi et al. 2013):

$$E_{\max,\text{synch}} \simeq 2.5 \times 10^8 m_e c^2 \left( \frac{\dot{E}}{10^{38.5} \text{ ergs/s}} \right)^{\frac{1}{6}} \left( \frac{\dot{N}}{10^{40} \text{ s}^{-1}} \right)^{-\frac{1}{3}} \left( \frac{\eta_B}{10^{-2.5}} \right)^{-\frac{1}{3}} \left( \frac{R_{\text{TS}}}{10^{17.5} \text{ cm}} \right)^{\frac{1}{3}} \quad (23)$$

and diffusion away from the termination shock,  $E_{\max,\text{conf}}$  (Sironi et al. 2013):

$$E_{\max,\text{conf}} \simeq 1.9 \times 10^7 m_e c^2 \left( \frac{\dot{E}}{10^{38.5} \text{ ergs/s}} \right)^{\frac{3}{4}} \left( \frac{\dot{N}}{10^{40} \text{ s}^{-1}} \right)^{-\frac{1}{2}}, \quad (24)$$

with the theoretical maximum energy  $E_{\max,\text{theory}}$  being the lower of the two. For all of our trials, diffusion is expected to limit the maximum energy of particles accelerated at the termination shock (i.e.,  $E_{\max,\text{theory}} = E_{\max,\text{conf}}$ ; Figure 13).

Since our model assumes that  $\dot{N} \propto \dot{E}$ ,  $E_{\max,\text{conf}}$  (and by extension,  $E_{\max,\text{theory}}$ ) depends strongly on the multiplicity  $\kappa$  of the pulsar wind, which is degenerate with minimum energy of particles injected into the PWN at the termination shock  $E_{\min}$  (Figure 9). As a result,  $E_{\max,\text{theory}}$  is highly degenerate with  $E_{\min}$  (Figure 14), and our model’s preference of  $E_{\min} \approx 10$  GeV (Table 4, Figure 10) suggests  $E_{\max,\text{theory}} \approx 15 - 25$  PeV. If acceleration at the termination shock can produce the highest energy particles required for a particular trial, then  $E_{\max} < E_{\max,\text{theory}}$ , a condition satisfied in for  $< 1/2$  of our trials (Figure 14).

The assumption that  $\dot{N} \propto \dot{E}$  results in  $E_{\max,\text{conf}} \propto \dot{E}^{\frac{1}{4}}$ . Therefore  $E_{\max,\text{conf}}$  was highest at earlier times, and its initial value depends strongly on the braking index  $p$  and spin-down timescale  $\tau_{\text{sd}}$  of PSR J1930+1852 (Figure 15). If, at early times, the maximum energy of particles accelerated at the termination shock is also limited by diffusion, this could be consistent with the high maximum particle energy  $E_{\max}$  required by many of the trials which accurately reproduce the observed properties of G54.1+0.3. However, even at early times, particle acceleration at the termination shock is insufficient to explain the maximum energy for most trials (Figure 15).

Lastly, numerical simulations suggests that spectral shape of particles accelerated at the termination shock depends strongly on the structure of the pulsar wind (e.g., Sironi & Spitkovsky 2011). When it leaves the neutron star magnetosphere, the pulsar wind is expected to be a primarily equatorial, and comprised of regions of alternating the magnetic field directions (e.g., Bogovalov 1999). The shape of the particle spectrum accelerated at the termination shock is expected to depend on the width of these magnetic “stripes”  $\lambda$  relative to the relativistic Larmor radius  $r_L$  and magnetization  $\sigma$  of the unshocked pulsar wind (Equation 3 in Sironi & Spitkovsky 2011):

$$\frac{\lambda}{r_L \sigma} \simeq 4\pi\kappa \frac{R_{\text{LC}}}{R_{\text{TS}}}, \quad (25)$$

where  $\kappa$  is the multiplicity (Equation 15),  $R_{\text{TS}}$  is the radius of the termination shock,  $R_{\text{LC}}$  is the radius of the light cylinder:

$$R_{\text{LC}} = \frac{cP}{2\pi}, \quad (26)$$

where  $P$  is the neutron star’s rotational period and  $c$  is the speed of light, and  $R_{\text{TS}}$  is the radius of termination shock. Specifically,  $\lambda/(r_L \sigma) \gtrsim 10$  is required for the spectrum of particles accelerated at the termination shock to resemble the broken power-law required by our model, otherwise their spectrum should be well approximated by a relativistic Maxwellian which our analysis disfavors (§2).

We can test this prediction using our trial parameters and the observed properties of this system. The measured  $P \approx 136.86$  ms and  $\dot{P} \approx 7.51 \times 10^{-13}$  s/s (Camilo et al. 2002) suggests that currently  $\dot{N}_{\text{GJ}} \approx 4.69 \times 10^{34}$  s<sup>-1</sup> and  $R_{\text{LC}} \approx 6.53 \times 10^8$  cm. Additionally, analysis of a *Chandra* observation identified a ring with semi-major axis  $\theta_{\text{TS}} = 5''7$  centered on PSR J1830+1852 associated with the termination shock in this source (Lu et al. 2002; Temim et al. 2010). For these values, the trial parameters with the lowest  $\chi^2$  favor  $\frac{\lambda}{r_L \sigma} \ll 1$  (Figure 16), in contradiction with the results of Sironi & Spitkovsky (2011). This

discrepancy is due to the relatively low multiplicity  $\kappa$  favored by our model which, as discussed above, results from the fitted value of  $E_{\min}$  (Figure 9).

It is important to note that our model does not consider the implications of ions in the pulsar wind, nor the possibility of magnetic reconnection and particle acceleration downstream of the pulsar wind as predicted by recent 3D simulations of these systems (e.g., Porth et al. 2013, 2014). These processes are expected to primarily affect the spectral evolution of the PWN (e.g., Olmi et al. 2014), and are left for future work.

## 5. Observational Tests

While our evolutionary model for a PWN inside a SNR (§2) reproduces the observed properties of G54.1+0.3 for a wide range in parameter space (Table 4), this is not necessarily statistically meaningful since there are an equal number of model parameters and observables (Table 3). Therefore, it is important to test the validity of this model by predicting the value of additional observable properties. Thanks to our parameter exploration, not only can we predict the values of future observations, we can also estimate the resulting improvement in the allowed physical parameters. For these predictions, we only use trials with  $\chi^2 < 7.09$ ,  $M_{\text{ej}} < 20 M_{\odot}$ , and  $p < 3.0$ . This maximum  $\chi^2$  is three higher than the lowest  $\chi^2$  of our MCMC trials, so we are investigating  $3\sigma$  parameter space. We only consider trials with  $M_{\text{ej}} < 20 M_{\odot}$  since stellar evolution models suggests this is the maximum ejecta mass possible for a Solar metallicity star (Heger et al. 2003; Woosley et al. 2002; Heger, private communication). Lastly, we only consider trials with  $p < 3$  since  $p > 3$  has yet to be measured from any isolated neutron star (e.g., Livingstone 2011).

As discussed in §3.1, while evidence for a SNR around G54.1+0.3 exists at both radio (Lang et al. 2010) and X-ray energies (Bocchino et al. 2010), many of its properties

remain unmeasured but whose values our model can predict. The age  $t_{\text{age}}$ , initial kinetic energy  $E_{\text{sn}}$  and mass  $M_{\text{ej}}$  of the supernova ejecta, and ISM density  $n_{\text{ism}}$  to predict the SNR expansion velocity  $v_{\text{snr}}$  of each trial. Due to the preferred young age and low ISM density, our model predicts an extremely high  $v_{\text{snr}} \gtrsim 30,000 \text{ km s}^{-1}$  (Figure 17). If this SNR is truly expanding this quickly, then electrons heated at the shock driven expanding ejecta will be significantly cooler than the shock-heated ions (Ghavamian et al. 2007), qualitatively consistent with a thermal interpretation of the SNR X-ray emission (Bocchino et al. 2010). Additionally, shocks with such extreme speeds are expected to efficiently accelerate both electron and proton to high energies (e.g., Kang & Jones 2005), consistent with the non-thermal interpretation of the observed X-ray emission (Bocchino et al. 2010). However, the fact that  $v_{\text{snr}}$  is significantly higher than that measured or inferred for any other SNR (e.g., Ghavamian et al. 2007) suggests the identified radio and X-ray shell may not actually be a SNR. If not, it could be the stellar wind bubble produced by the progenitor star, which is expected to be  $\theta_b \sim 2'.7 - 14'$  in size (§4.1). Measuring the spectrum of both the diffuse X-ray emission and radio shell around G54.1+0.3 are required to determine if this emission is from a SNR or a stellar wind bubble. If future studies indicate this emission is from a stellar wind bubble and not a SNR as assumed here, our model would still favor a  $\sim 15 - 20 M_\odot$  progenitor based on the properties of the IR emission around the PWN (§4.1). However, it would limit our ability to constrain the ISM density.

While there have been numerous observations of G54.1+0.3 across the electromagnetic spectrum (§3.1), there still remains additional quantities which, if measured, would not only test the accuracy of the evolutionary model described in §2 significantly improve our understanding of this source. Since our model requires the PWN has yet to collide with the SNR reverse shock (§4.1, Figure 7), the rate at which the average angular radius of the PWN expands  $\dot{\theta}_{\text{pwn}}$  is sensitive to the mass  $M_{\text{ej}}$  and initial kinetic energy  $E_{\text{sn}}$  of the supernova ejecta, and is  $\dot{\theta}_{\text{pwn}} \sim 20 - 50 \text{ mas year}^{-1}$  for the preferred value of these

parameters (Figure 18). Therefore, radio observations  $\sim 5 - 10$  years apart could detect its expansion, though such measurements are complicated by its considerable asymmetry (Lang et al. 2010).

Additional, we can predict the properties of the source at low ( $< 300$  MHz) radio frequencies, which can be measured by new facilities like LOFAR (van Haarlem et al. 2013). Using our model, we calculate the 60 MHz ( $S_{60}$ ) and 150 MHz ( $S_{150}$ ) flux densities and the 30 – 80 MHz ( $\alpha_{30-80}$ ) and 120 – 240 MHz ( $\alpha_{120-240}$ ) spectral indices ( $S_\nu \propto \nu^\alpha$ ) of this PWN for those trials which have “realistic” parameters as defined above. We find that the flux densities in both bands are useful for determining the distance  $d$  to G54.1+0.3 as well as the braking index  $p$ , spin-down timescale  $\tau_{\text{sd}}$  and initial spin period  $P_0$  of PSR J1930+1852 (Figure 19), while the spectral indices are sensitive to the minimum energy of particles injected into the PWN at the termination shock  $E_{\min}$  (Figure 20).

Similar results can be gained by studying the hard X-ray emission from PWN G54.1+0.3, and we predicts its properties from 5 – 80 keV since this is the energy range detectable with the recently launched *NuSTAR* satellite (Harrison et al. 2013). The flux in this energy range can not only help constrain the break energy  $E_{\text{break}}$  and high-energy index  $p_2$  of particles injected into the PWN at the termination shock, but – due to the degeneracies discussed in §3.2 – strongly depends on the distance to this source (Figure 21). Additionally, the photon index in this range  $\Gamma_{5-80}$  depends on the maximum energy  $E_{\text{break}}$  and high-energy index  $p_2$  of particles injected into the PWN at the termination shock (Figure 22).

## 6. Summary and Conclusions

In summary, we have fit the observed properties of G54.1+0.3 using a one-zone model for the evolution of a PWN inside a SNR (§2). This model can reproduce its observed properties (§3.1), and suggests that the progenitor was an isolated  $\sim 05 M_{\odot}$  star, most likely the member of a massive star cluster, which exploded in a low density environment possibly produced by its stellar wind (§4.1). The resultant neutron star, PSR J1930+1852, had an initial spin period  $P_0 \sim 30 - 80$  ms (§4.2). Our model requires that the current multiplicity of particle production in its magnetosphere is  $\kappa \sim (1 - 3) \times 10^5$ , and suggest that the magnetosphere electric potential is sufficient to accelerate particles to the highest energies  $E_{\max}$  required by our model. The low magnetization of the pulsar wind and low-energy component of particle spectrum can be attributed to acceleration resulting from magnetic reconnection between the light cylinder and the termination shock, though our model suggests the “stripes” in the unshocked pulsar wind are too narrow for acceleration at the termination shock to produce the broken power-law spectrum required by our modeling. These results can be tested with radio and X-ray observations of this source, which can better determine the initial spin period PSR J1930+1852, the properties of particles accelerated in this source, and the nature of the extended radio and X-ray emission surrounding this PWN.

JDG will like to thank Erin Sheldon for the IDL code used in the MCMC fits, Kaisey Mandel and David Hogg for useful discussions concerning MCMC fitting, Ester Aliu for information regarding the GeV spectrum, and Roger Chevalier, Vikram Dwarkadas, Daniel Patnaude, and Lorenzo Sironi for useful advice.

OBSERVABLE	VALUE	REFERENCE
Distance	4.5 – 9 kpc	Leahy et al. (2008)
<i>Pulsar Properties</i>		
Current spin-down luminosity $\dot{E}$	$1.2 \times 10^{37} \frac{\text{ergs}}{\text{s}}$	Camilo et al. (2002)
Characteristic Age $t_{\text{ch}}$	2900 years	Camilo et al. (2002)
<i>Supernova Remnant Properties</i>		
Angular Radius $\theta_{\text{snr}}$	$6'.6 \pm 0'.4$	Lang et al. (2010) Bocchino et al. (2010)
<i>Pulsar Wind Nebula Properties</i>		
Angular Radius $\theta_{\text{pwn}}$	$1'.14 \pm 0'.04$	Lang et al. (2010)
1.4 GHz Flux Density	$433 \pm 30 \text{ Jy}$	Lang et al. (2010)
4.7 GHz Flux Density	$327 \pm 25 \text{ Jy}$	Lang et al. (2010)
8.5 GHz Flux Density	$252 \pm 20 \text{ Jy}$	Lang et al. (2010)
2–10 keV Unabsorbed X-ray Flux $F_{\text{X},2-10}$	$(5.43 \pm 0.035) \times 10^{-12} \frac{\text{ergs}}{\text{s cm}^2}$	Temim et al. (2010)
X-ray Photon Index $\Gamma$	$2.09 \pm 0.01$	Temim et al. (2010)
311 GeV Photon Density	$(1.10 \pm 0.56) \times 10^{-11} \frac{\text{photons}}{\text{cm}^2 \text{ s TeV}}$	Acciari et al. (2010)
492 GeV Photon Density	$(4.2 \pm 1.4) \times 10^{-12} \frac{\text{photons}}{\text{cm}^2 \text{ s TeV}}$	Acciari et al. (2010)
780 GeV Photon Density	$(1.12 \pm 0.45) \times 10^{-12} \frac{\text{photons}}{\text{cm}^2 \text{ s TeV}}$	Acciari et al. (2010)
1.2 TeV Photon Density	$(6.2 \pm 1.7) \times 10^{-13} \frac{\text{photons}}{\text{cm}^2 \text{ s TeV}}$	Acciari et al. (2010)
3 TeV Photon Density	$(3.9 \pm 2.1) \times 10^{-14} \frac{\text{photons}}{\text{cm}^2 \text{ s TeV}}$	Acciari et al. (2010)

Table 1: Observed Properties of PWN G54.1+0.3

PARAMETER	DESCRIPTION	UNITS
$E_{\text{sn}}$	Initial Kinetic Energy of Supernova Ejecta	ergs
$M_{\text{ej}}$	Mass of Supernova Ejecta	Solar Masses
$n_{\text{ism}}$	Number Density of Surrounding Interstellar Medium	$\text{cm}^{-3}$
$p$	Neutron Star Braking Index	...
$\tau_{\text{sd}}$	Neutron Star Spin-down Timescale	years
$\eta_B$	Magnetization of Pulsar Wind	...
$E_{\text{min}}$	Minimum Injection Energy	GeV
$E_{\text{break}}$	Break Energy in Injection Spectrum	GeV
$E_{\text{max}}$	Maximum Injection Energy	GeV
$p_1$	Particle Index for $E_{\text{min}} < E < E_{\text{break}}$	...
$p_2$	Particle Index for $E_{\text{break}} < E < E_{\text{max}}$	...
$d$	Distance to PWN G54.1+0.3	kpc

Table 2: Fit parameters in the model fit to observed properties of PWN G54.1+0.3

Model Input Parameters		Predicted Observables		
Parameter	Value	Observable	OBSERVED VALUE	PREDICTED VALUE
$\log(E_{\text{sn}}/10^{51} \text{ ergs})$	-0.03	$\theta_{\text{snr}}$	$6.6 \pm 0.4$	6.5
$\log(M_{\text{ej}}/M_{\odot})$	1.34	$\theta_{\text{pwn}}$	$1.14 \pm 0.04$	1.12
$\log(n_{\text{ism}}/\text{cm}^{-3})$	-2.29	1.4 GHz Flux Density	$433 \pm 30 \text{ Jy}$	429 Jy
Distance [kpc]	4.90	4.7 GHz Flux Density	$327 \pm 25 \text{ Jy}$	329 Jy
$p$	2.94	8.5 GHz Flux Density	$252 \pm 20 \text{ Jy}$	257 Jy
$\log(\tau_{\text{sd}}/1 \text{ year})$	2.90	$F_{\text{X},2-10}$	$(5.43 \pm 0.035) \times 10^{-12} \frac{\text{ergs}}{\text{s cm}^2}$	$5.43 \times 10^{-12} \frac{\text{ergs}}{\text{s cm}^2}$
$\log(\eta_{\text{B}})$	-3.14	$\Gamma$	$2.09 \pm 0.01$	$2.09 \pm 0.002$
$\log(E_{\text{min}}/\text{GeV})$	1.05	311 GeV Photon Density	$(1.10 \pm 0.56) \times 10^{-11} \frac{\text{photons}}{\text{cm}^2 \text{ s TeV}}$	$0.80 \times 10^{-11} \frac{\text{photons}}{\text{cm}^2 \text{ s TeV}}$
$\log(E_{\text{break}}/\text{GeV})$	3.45	492 GeV Photon Density	$(4.2 \pm 1.4) \times 10^{-12} \frac{\text{photons}}{\text{cm}^2 \text{ s TeV}}$	$3.1 \times 10^{-12} \frac{\text{photons}}{\text{cm}^2 \text{ s TeV}}$
$\log(E_{\text{min}}/\text{GeV})$	6.98	780 GeV Photon Density	$(1.12 \pm 0.45) \times 10^{-12} \frac{\text{photons}}{\text{cm}^2 \text{ s TeV}}$	$1.21 \times 10^{-12} \frac{\text{photons}}{\text{cm}^2 \text{ s TeV}}$
$p_1$	1.84	1.2 TeV Photon Density	$(6.2 \pm 1.7) \times 10^{-13} \frac{\text{photons}}{\text{cm}^2 \text{ s TeV}}$	$4.9 \times 10^{-13} \frac{\text{photons}}{\text{cm}^2 \text{ s TeV}}$
$p_2$	2.77	3 TeV Photon Density	$(3.9 \pm 2.1) \times 10^{-14} \frac{\text{photons}}{\text{cm}^2 \text{ s TeV}}$	$7.2 \times 10^{-14} \frac{\text{photons}}{\text{cm}^2 \text{ s TeV}}$

Table 3: Predicted values for the observable quantities listed in Table 1 for the set of model parameters with the lowest  $\chi^2$ .

PARAMETER	This work	Chevalier (2005)	Bocchino et al. (2010)	Li et al. (2010)	Tanaka & Takahara (2011)	Torres et al. (2014)
$E_{\text{sn}}$ [ $10^{51}$ ergs]	$0.08 - 1.5$	$\equiv 1$	$0.3 - 1.6$	...	...	$\equiv 1$
$M_{\text{ej}}$ [ $M_{\odot}$ ]	$5.7 - 44$	$\equiv 5$	$\equiv 8$	...	...	$\equiv 20$
$n_{\text{ism}}$ [ $\text{cm}^{-3}$ ]	$(0.03 - 6.3) \times 10^{-3}$	...	$\sim 0.2$	...	...	$\equiv 10$
Distance [kpc]	$4.6 - 8.1$	$\sim 5$	$\equiv 6.2$	$\equiv 6.2$	$\equiv 6.2$	$\equiv 6$
Braking Index $p$	$1.90 - 2.93$	$\equiv 3$	$\equiv 3$	$\equiv 3$	$\equiv 3$	$\equiv 3$
$\tau_{\text{sd}}$ [years]	$280 - 3500$	$\approx 1400$	$\equiv 3$	...	$600 / 1200$	$1171$
$\eta_B$	$(0.44 - 2.2) \times 10^{-3}$	$\equiv \frac{3}{7}$	...	$\sim 1.5 \times 10^{-3}$	$0.3 \times 10^{-3} / 2 \times 10^{-3}$	$5 \times 10^{-3}$
$E_{\text{min}}$ [GeV]	$0.31 - 15$	...	...	$\equiv 0.05$	$< 10$	...
$E_{\text{break}}$ [TeV]	$0.71 - 11$	...	...	$\equiv 0.26$	$0.15 / 0.09$	$0.3$
$E_{\text{max}}$ [PeV]	$0.96 - 2700$	...	...	Variable	$> 0.5$	$0.38$ (Variable)
$p_1$	$1.43 - 2.08$	$\equiv 1.26$	...	$\equiv 1.2$	1.2	1.2
$p_2$	$2.60 - 2.78$	$\equiv 2.8$	...	$\sim 2.8$	2.55	2.8
Age [years]	$2100 - 3600$	$\approx 1500$	$1800 - 3300$	$\sim 2900$	$2300 / 1700$	$1700$
$\dot{E}_0$ [ergs s $^{-1}$ ]	$(0.06 - 2.5) \times 10^{39}$	$\approx 5.1 \times 10^{37}$	$\equiv 4 \times 10^{38}$	$\equiv 1.4 \times 10^{39}$	$2.9 \times 10^{38} / 6.9 \times 10^{37}$	$7.2 \times 10^{37}$
$P_0$ [ms]	$32 - 84$	$\approx 100$	$\equiv 56$	...	$62 / 87$	87

Table 4: The 90% confidence interval of the properties of G54.1+0.3 derived from our analysis, compared with values derived from previous analyses of this source. Chevalier (2005) do not specify a braking index  $p$  for this neutron star, and the quoted values of  $\tau_{\text{sd}}$  and  $\dot{E}_0$  are calculated assuming  $p \equiv 3$  for the age derived in their analysis. As described in §3.2.1, Tanaka & Takahara (2011) calculate the properties of this PWN assuming two different energy densities of the background IR photon field, with the values to the left of the “/” inferred for a lower energy density while the values to the right are those inferred for a higher energy density.

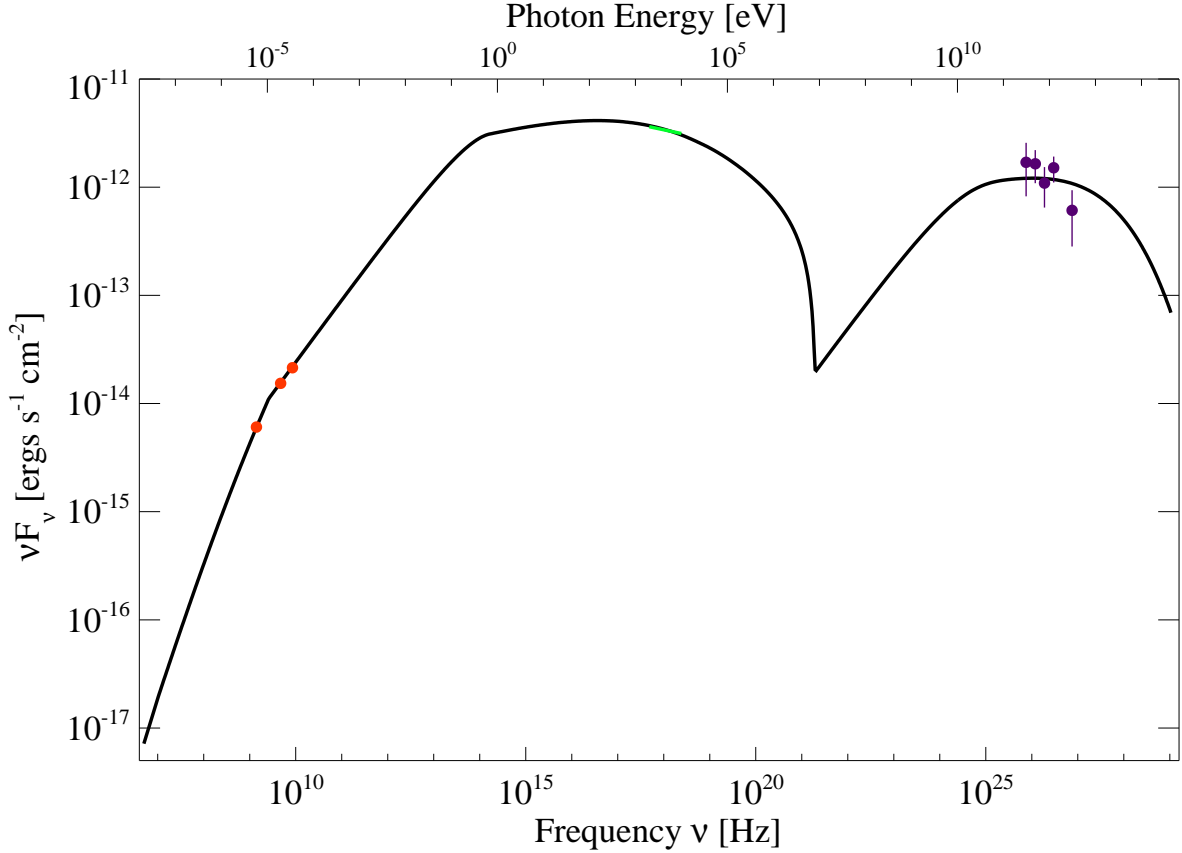


Fig. 1.— The broadband spectral energy diagram of PWN G54.1+0.3 predicted by the model described in §2 for the parameters listed in Table 2. The red, green, and purple points are, respectively, the observed radio, X-ray, and TeV  $\gamma$ -ray emission (§3.1, Table 1).

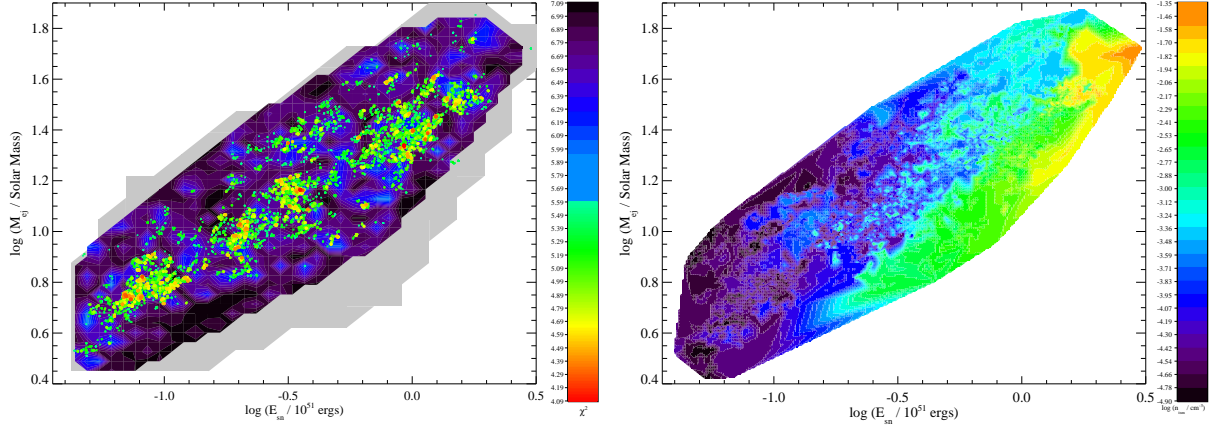


Fig. 2.— *Top:* Trial values of the initial kinetic energy  $E_{\text{sn}}$  and mass  $M_{\text{ej}}$  of the supernova ejecta in G54.1+0.3, with the color indicating the  $\chi^2$  of a particular trial where red signifies a lower  $\chi^2$  (better fit) and black signifies a higher  $\chi^2$  (worse fit). *Bottom:* Value of the ISM density  $n_{\text{ism}}$  (color scale) as function of  $E_{\text{sn}}$  and  $M_{\text{ej}}$  for trials with  $\chi^2 < 7.09$ .

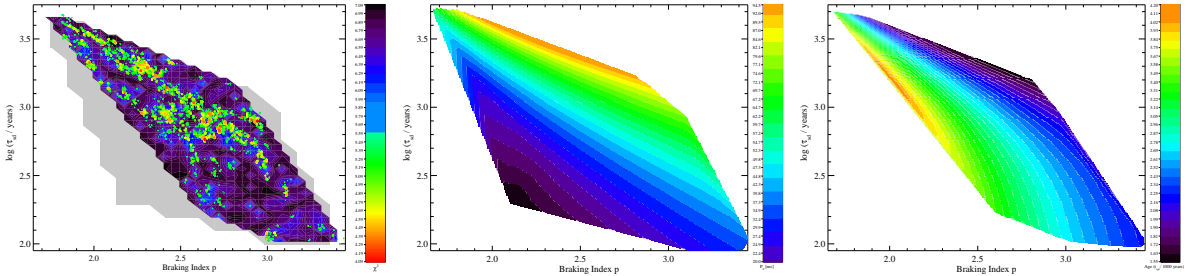


Fig. 3.— *Left:* Trial values of the braking index  $p$  and spin-down timescale  $\tau_{\text{sd}}$  of PSR J1930+1852 with the color indicating the  $\chi^2$  of a given trial, where red signifies a lower  $\chi^2$  (better fit) and black signifies a higher  $\chi^2$  (worse fit). Initial spin period  $P_0$  (*middle*) and age  $t_{\text{age}}$  (*right*) for trial values of the braking index  $p$  and spin-down timescale  $\tau_{\text{sd}}$ . Only the values for trials with  $\chi^2 < 7.09$  are shown.

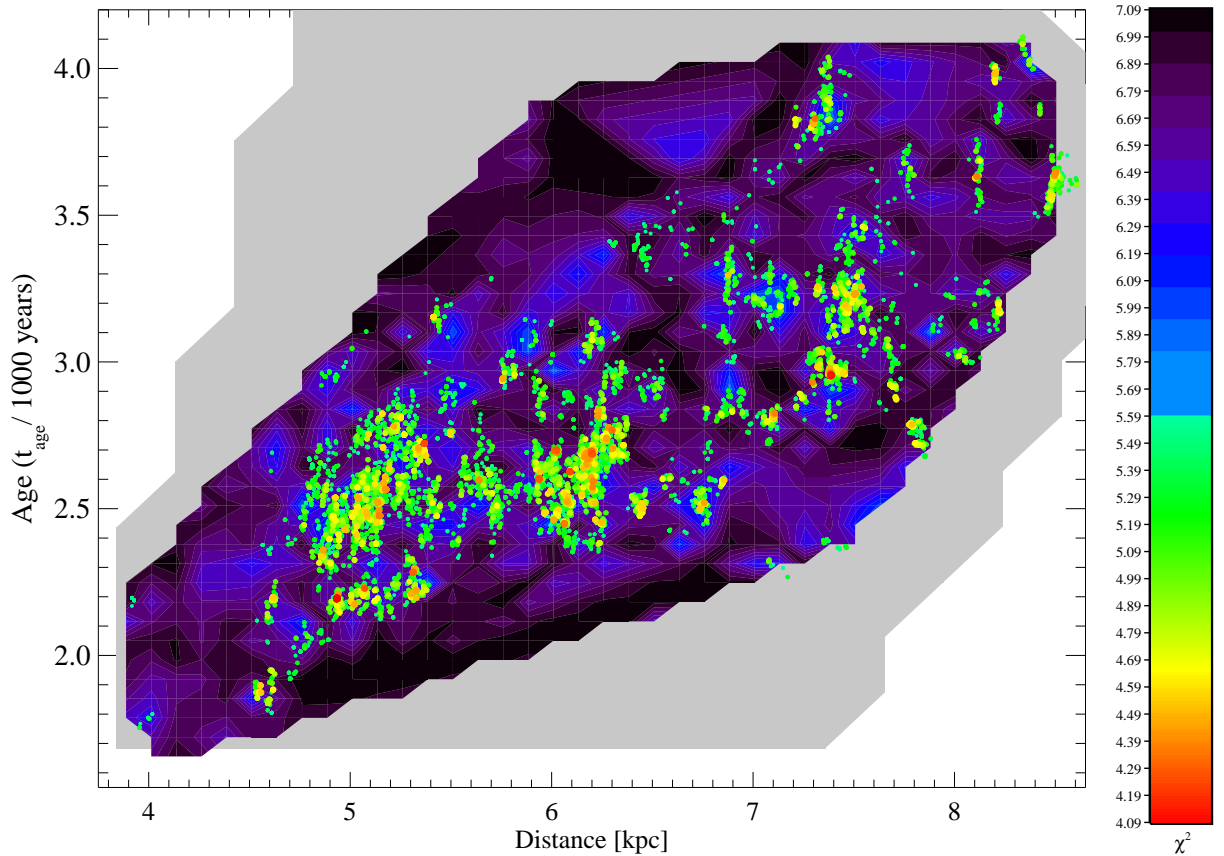


Fig. 4.— Trial values of the distance  $d$  to and age  $t_{\text{age}}$  of G54.1+0.3. The greyscale indicates the distribution the distribution of these parameters for trials with  $\chi^2 > 7.09$ , while color indicates trials with  $\chi^2 < 7.09$ , where red signifies a lower  $\chi^2$  (better fit) and black signifies a higher  $\chi^2$  (worse fit).

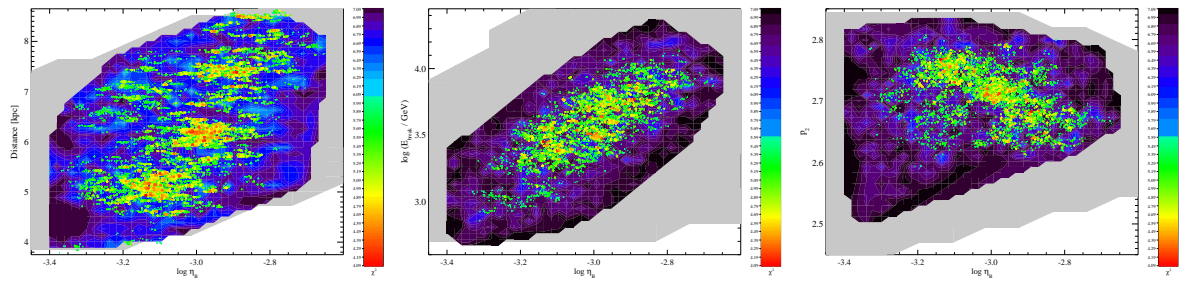


Fig. 5.— Trial values of the distance  $d$  (*left*), break energy  $E_{\text{break}}$  (*middle*), high-energy particle index  $p_2$  (*right*) and the wind magnetization  $\eta_B$  of G54.1+0.3. The greyscale indicates the distribution the distribution of these parameters for trials with  $\chi^2 > 7.09$ , while color indicates trials with  $\chi^2 < 7.09$ , where red signifies a lower  $\chi^2$  (better fit) and black signifies a higher  $\chi^2$  (worse fit).

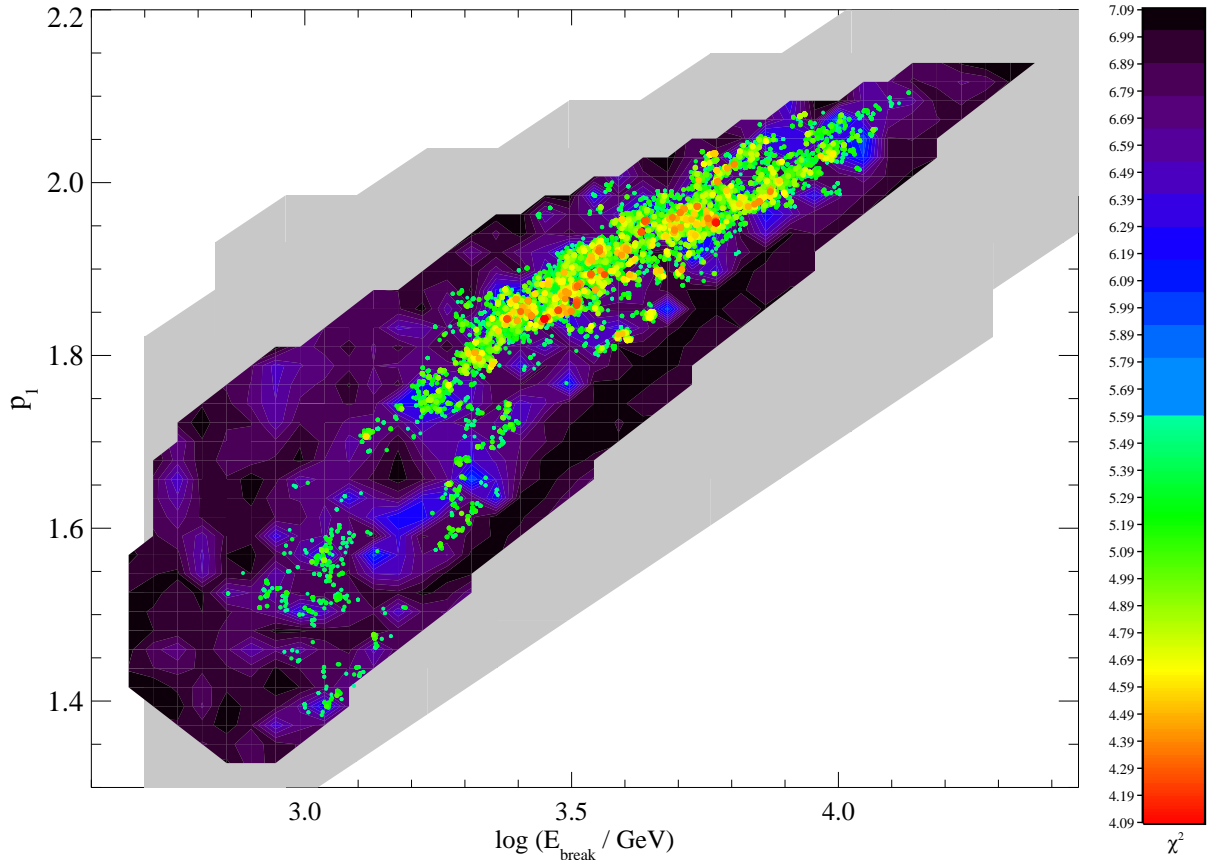


Fig. 6.— Trial values of the break energy  $E_{\text{break}}$  and low-energy particle index  $p_1$  of the pulsar wind in G54.1+0.3. The greyscale indicates the distribution of these parameters for trials with  $\chi^2 > 7.09$ , while color indicates trials with  $\chi^2 < 7.09$ , where red signifies a lower  $\chi^2$  (better fit) and black signifies a higher  $\chi^2$  (worse fit).

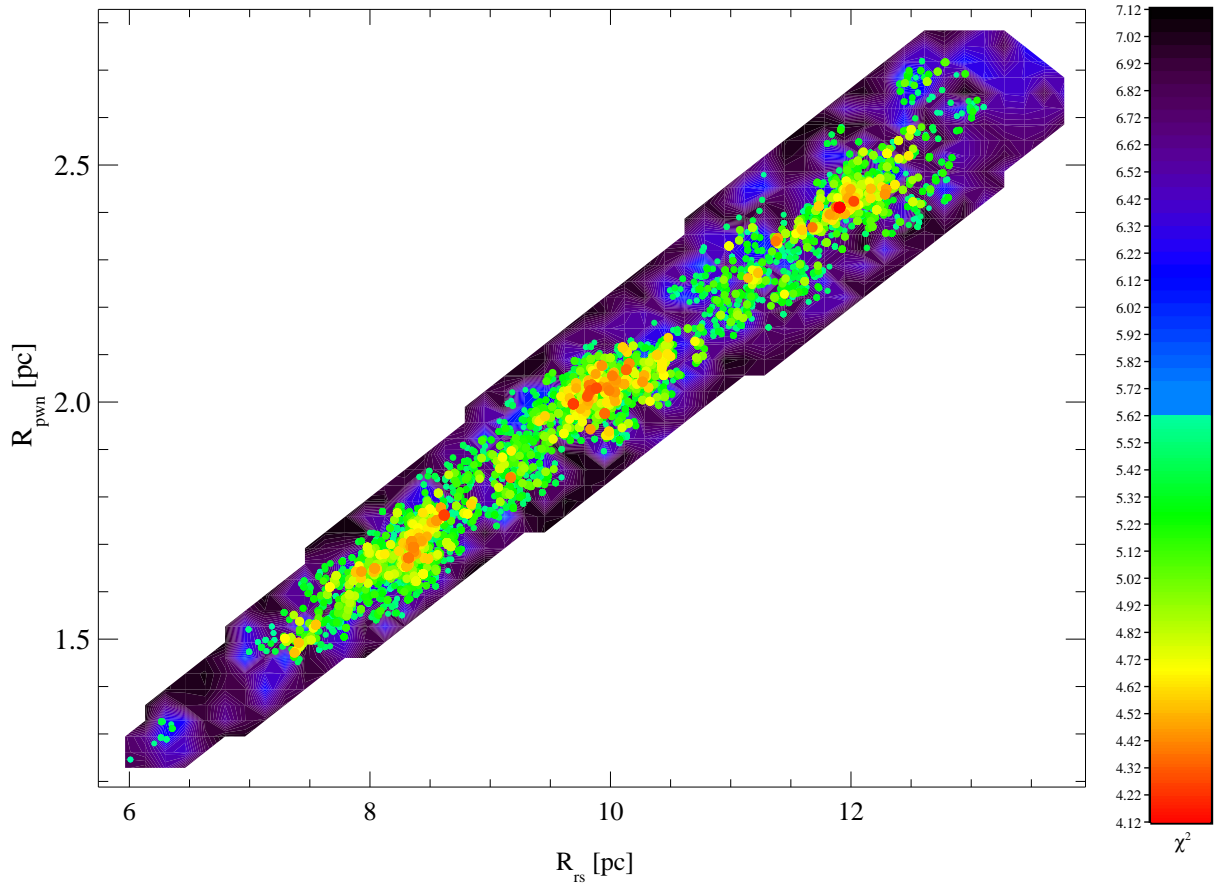


Fig. 7.— The expected radius of the SNR reverse shock  $R_{\text{rs}}$  and PWN  $R_{\text{pwn}}$  for MCMC trials with  $\chi^2 < 7.09$ ,  $M_{\text{ej}} < 20 M_{\odot}$ , and  $p < 3$ .

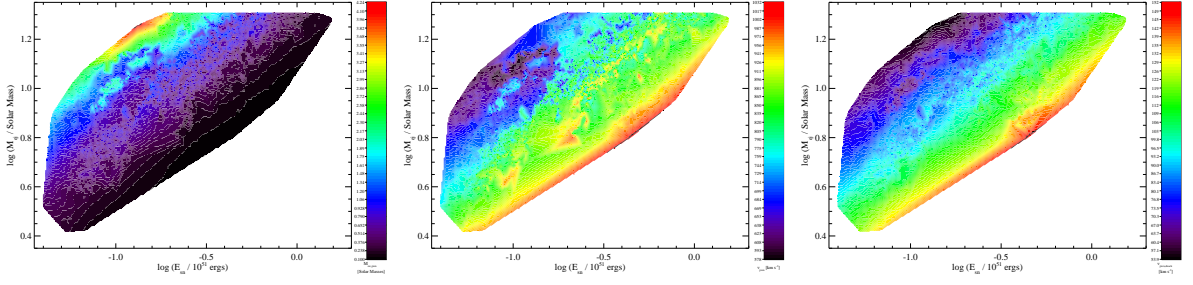


Fig. 8.— The expected mass of material swept-up by the PWN  $M_{\text{sw,pwn}}$  (*left*), PWN expansion speed  $v_{\text{pwn}}$  (*middle*), and PWN shock speed  $v_{\text{pwn,shock}}$  (*right*; Equation 10) as a function of the initial kinetic energy  $E_{\text{sn}}$  and mass  $M_{\text{ej}}$  of the supernova ejecta for MCMC trials with  $\chi^2 < 7.09$ ,  $M_{\text{ej}} < 20 M_\odot$ , and  $p < 3$ .

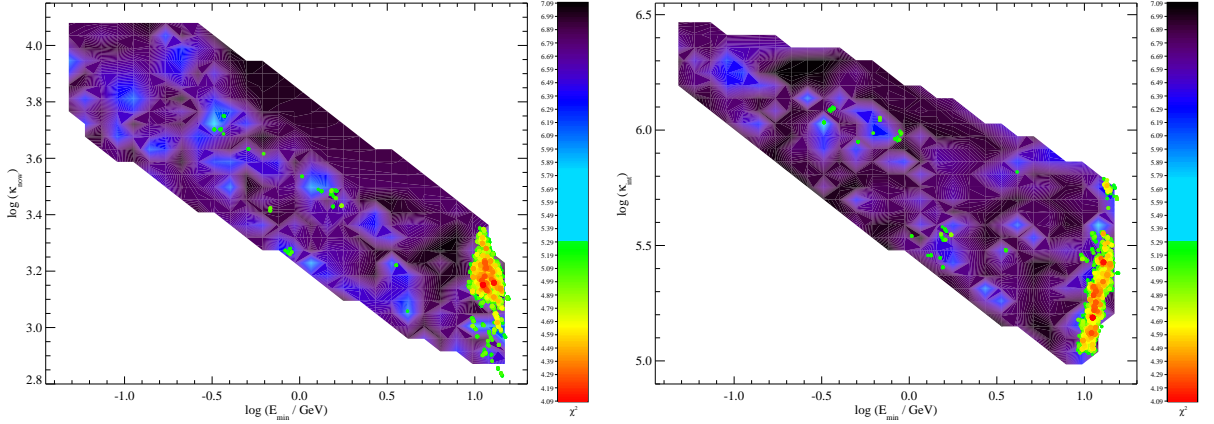


Fig. 9.— The current  $\kappa_{\text{now}}$  (Equation 15; *left*) and time-integrated  $\kappa_{\text{int}}$  (Equation 16; *right*) multiplicity of the pulsar wind for trial values of the minimum energy of particles injected at the termination shock  $E_{\text{min}}$ . The color indicates the  $\chi^2$  of each MCMC trial.

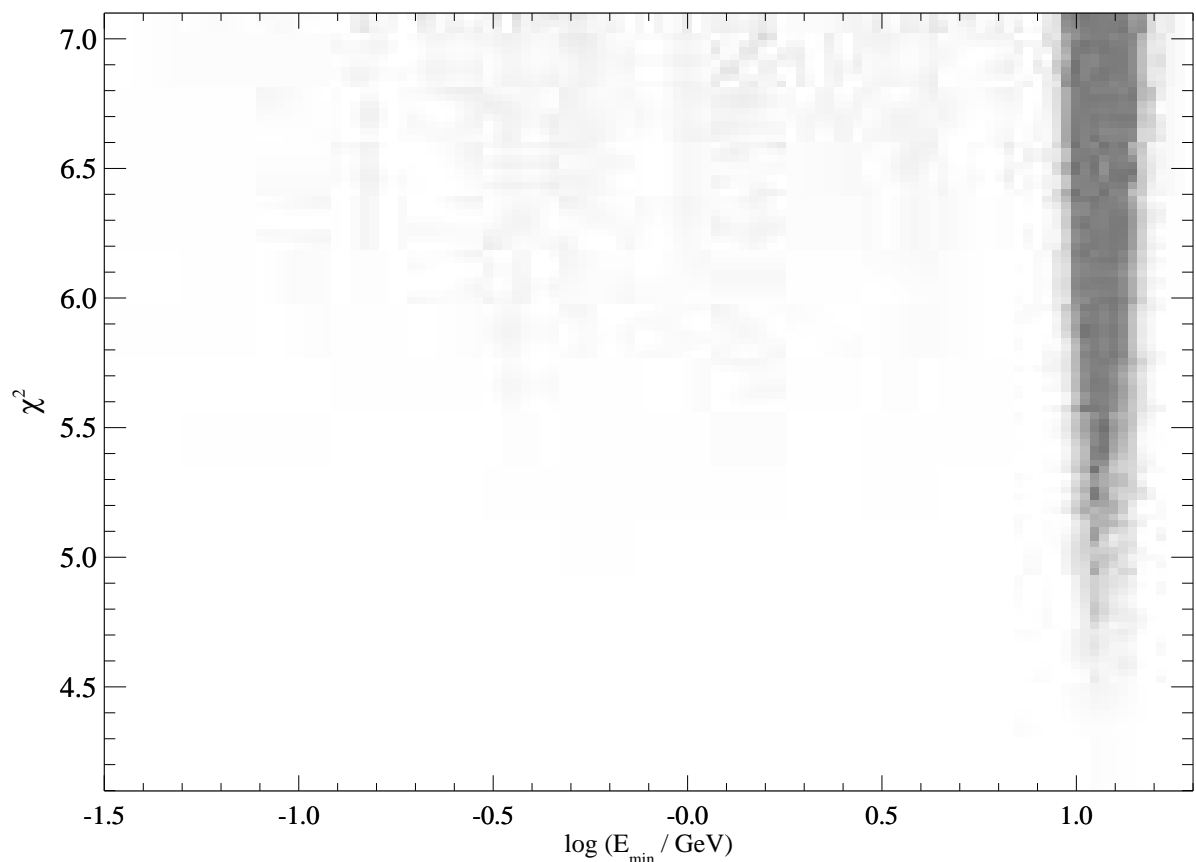


Fig. 10.—  $\chi^2$  for trial values of the minimum energy  $E_{\min}$  of the pulsar wind in G54.1+0.3.

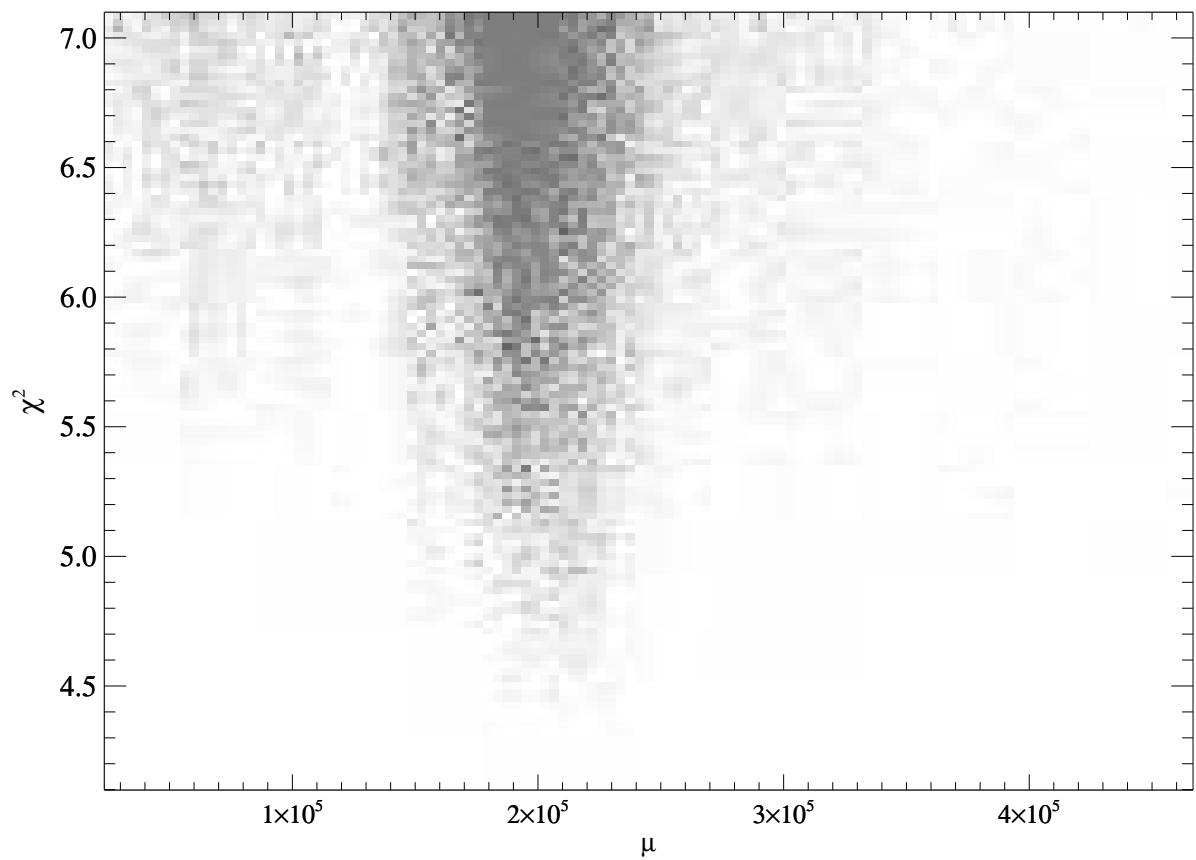


Fig. 11.—  $\chi^2$  for values of  $\mu$  (defined in Equation 18) for MCMC trials.

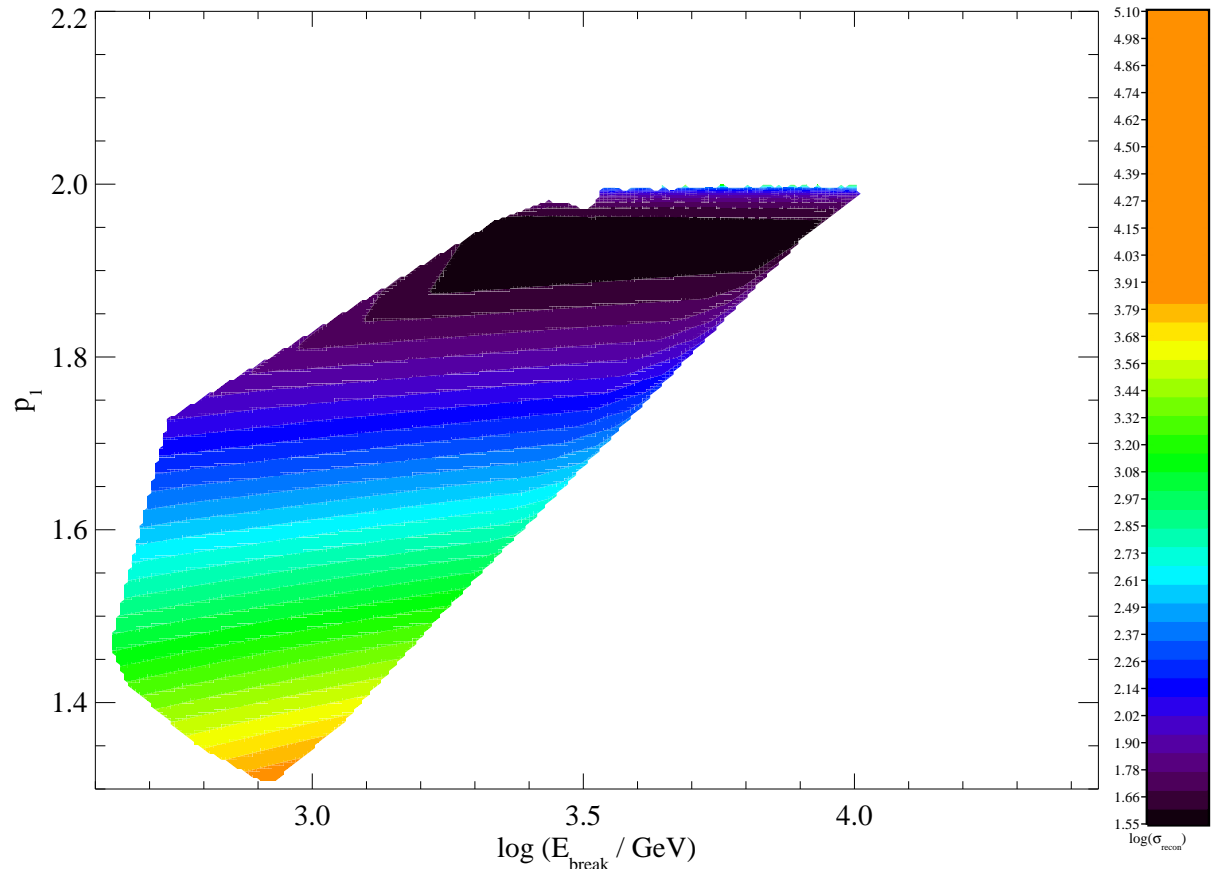


Fig. 12.— Value of  $\log(\sigma_{\text{recon}})$  (Equation 22) as a function of  $E_{\text{break}}$  and  $p_1$  from trials with a  $\chi^2 < 7.09$ .

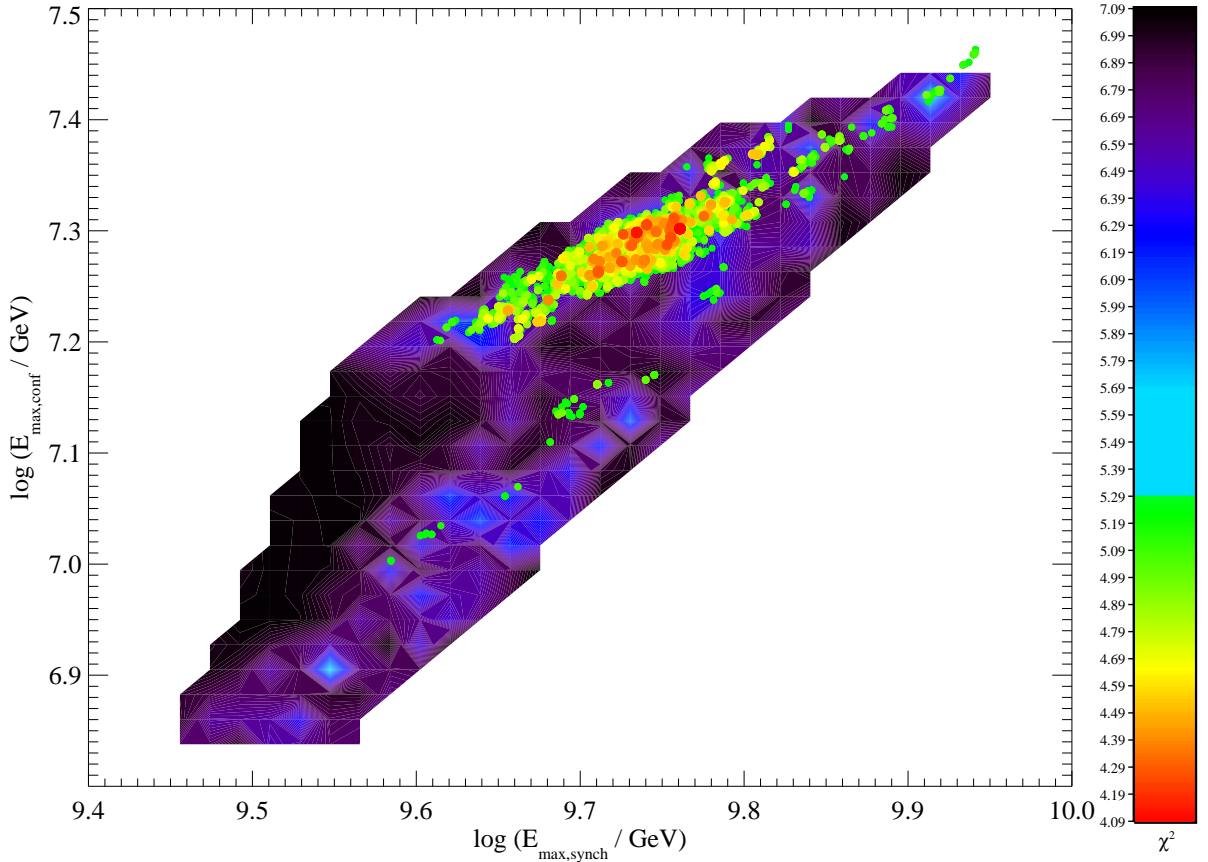


Fig. 13.— The expected maximum energy of particles accelerated at termination shock is limited by synchrotron losses ( $E_{\text{max,synch}}$ ; Equation 23) or confinement ( $E_{\text{max,conf}}$ ; Equation 24) for trials with  $\chi^2 < 7.09$ .

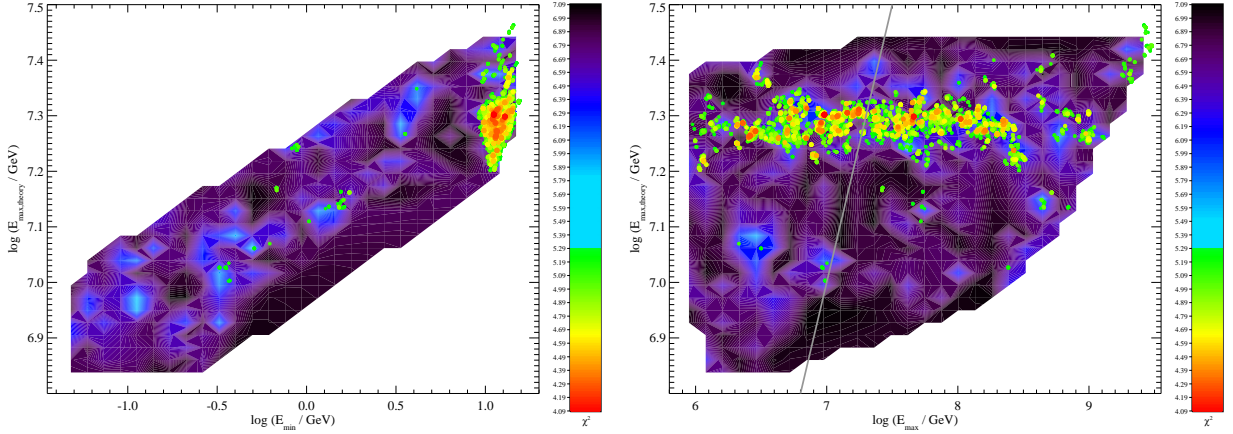


Fig. 14.— The theoretical maximum energy  $E_{\max, \text{theory}}$  of particles currently accelerated at termination shock as a function for the trial values of the minimum  $E_{\min}$  (*left*) and maximum  $E_{\max}$  (*right*) energy particles injected at the termination shock.

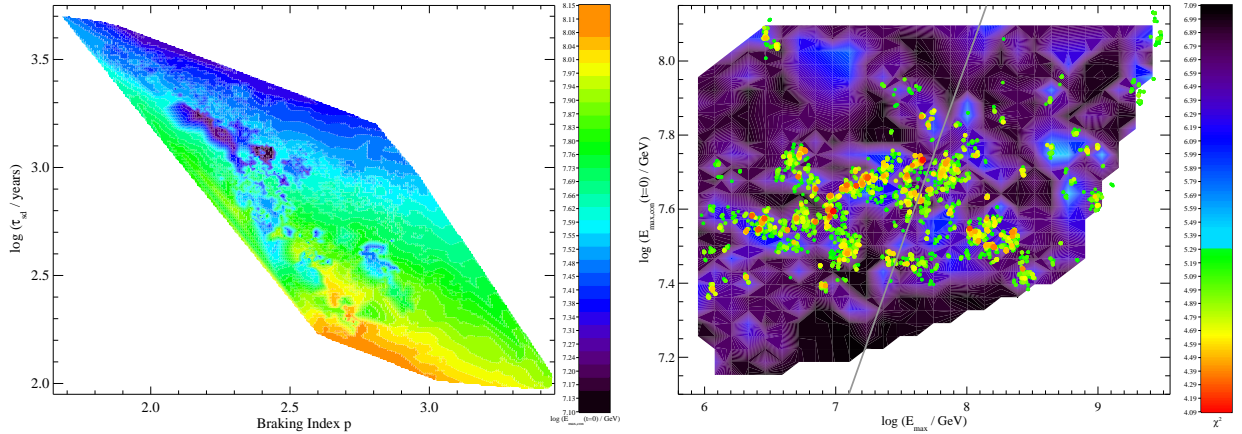


Fig. 15.— *Left:* Value of  $\log E_{\max, \text{conf}}(t = 0)$  (Equation 24) as a function of  $p$  and  $\tau_{\text{sd}}$  for trials with a  $\chi^2 < 7.09$ . *Right:* The maximum energy  $E_{\max}$  and the diffusion-limited maximum energy of particles currently accelerated at the termination shock at  $t = 0$ ,  $E_{\max, \text{conf}}(t = 0)$ , for trials with  $\chi^2 < 7.09$ . The gray line indicates  $E_{\max} = E_{\max, \text{conf}}(t = 0)$ , with points to the left of the line having  $E_{\max} < E_{\max, \text{conf}}(t = 0)$ .

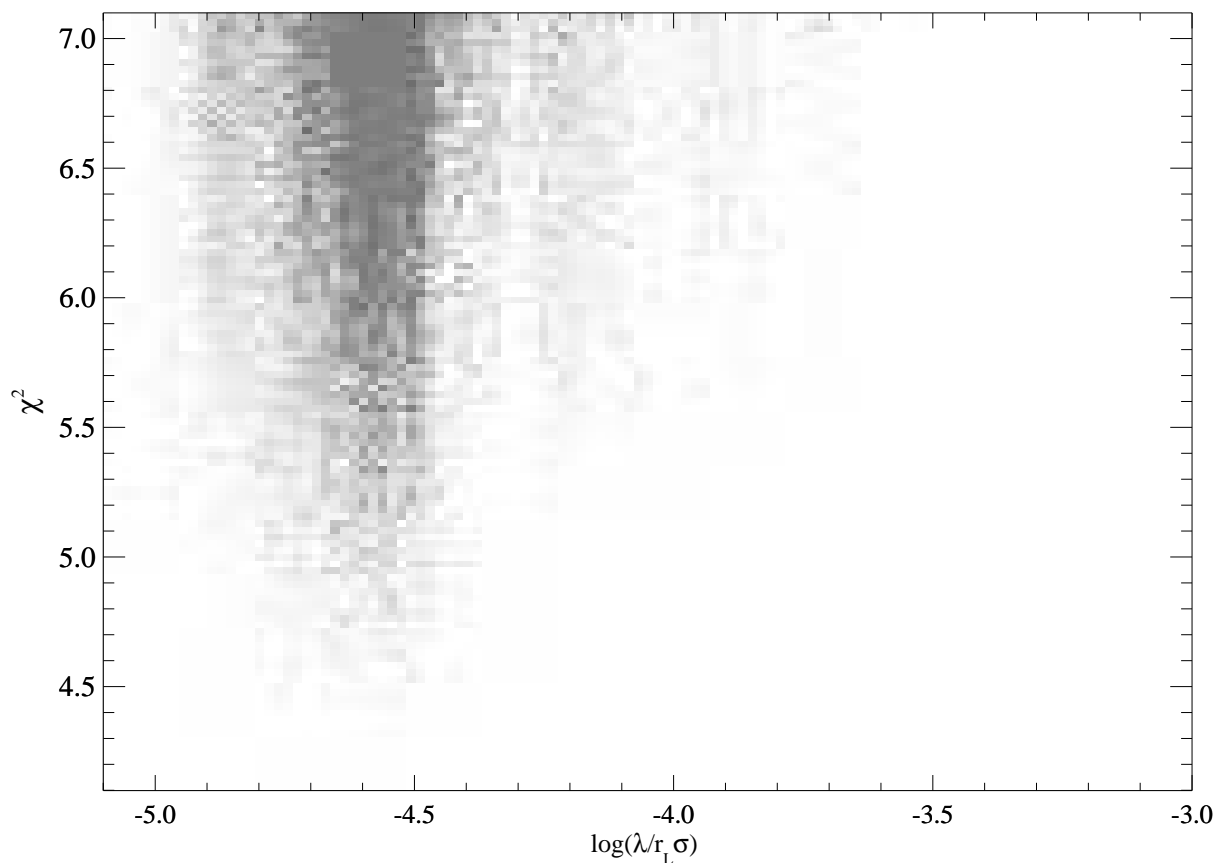


Fig. 16.—  $\chi^2$  for values of  $\log\left(\frac{\lambda}{r_L \sigma}\right)$  (defined in Equation 25) for MCMC trials.

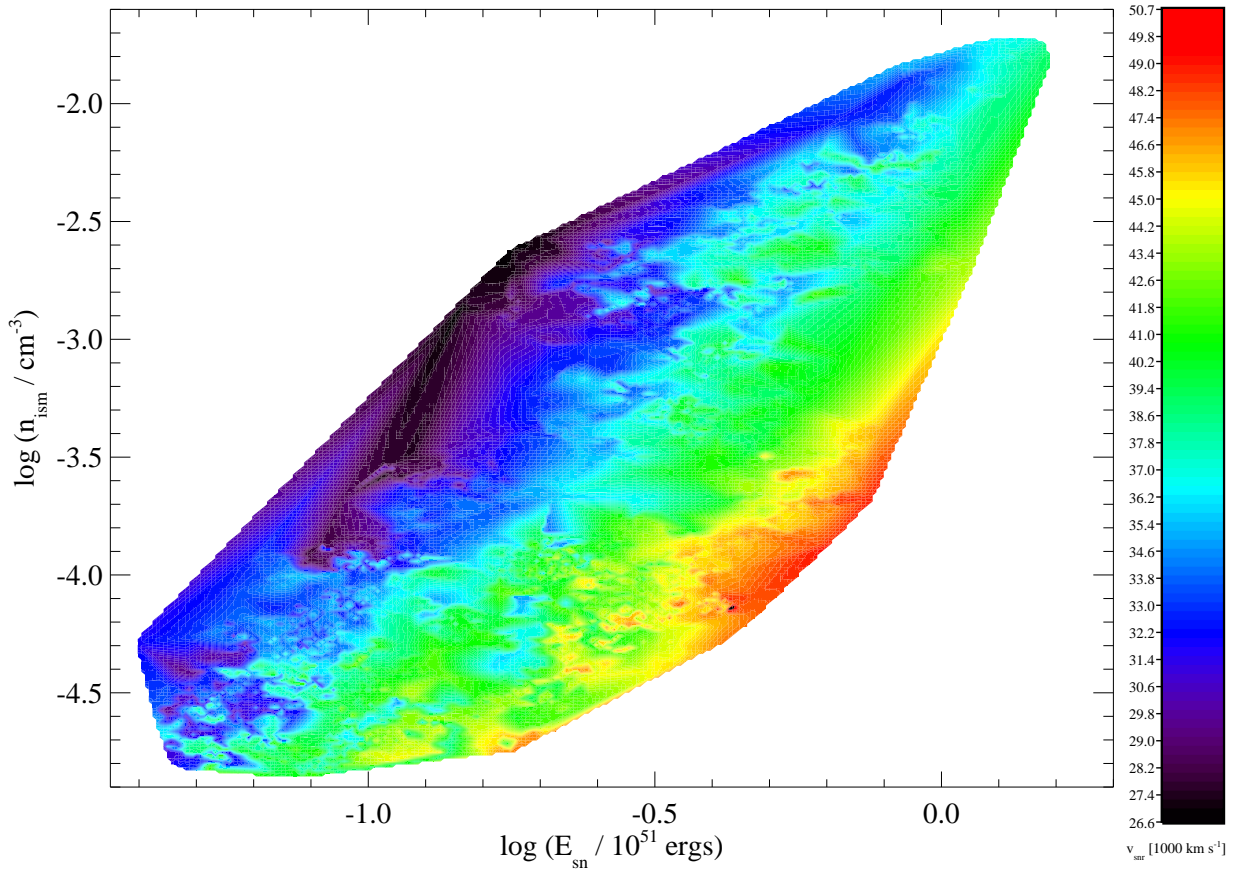


Fig. 17.— The expected SNR expansion speed  $v_{\text{snr}}$  as a function of supernova energies  $E_{\text{sn}}$  and ISM densities  $n_{\text{ism}}$  for MCMC trials with  $\chi^2 < 7.09$ ,  $M_{\text{ej}} < 20 M_{\odot}$ , and  $p < 3$ .

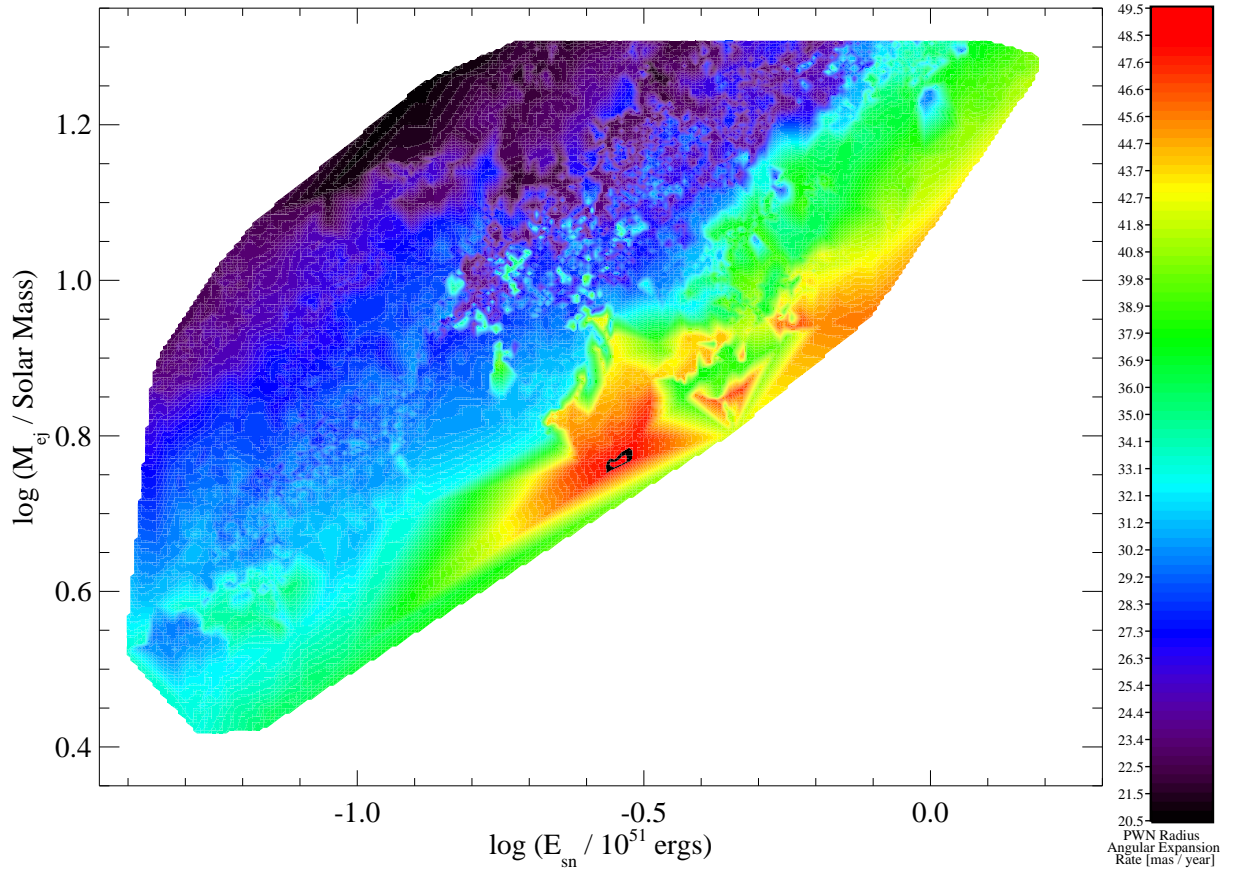


Fig. 18.— The expected angular expansion rate of this PWN’s radius  $\dot{\theta}_{\text{pwn}}$  as a function of the initial kinetic energy  $E_{\text{sn}}$  and mass  $M_{\text{ej}}$  of the supernova ejecta for MCMC trials with  $\chi^2 < 7.09$ ,  $M_{\text{ej}} < 20 M_{\odot}$ , and  $p < 3$ .

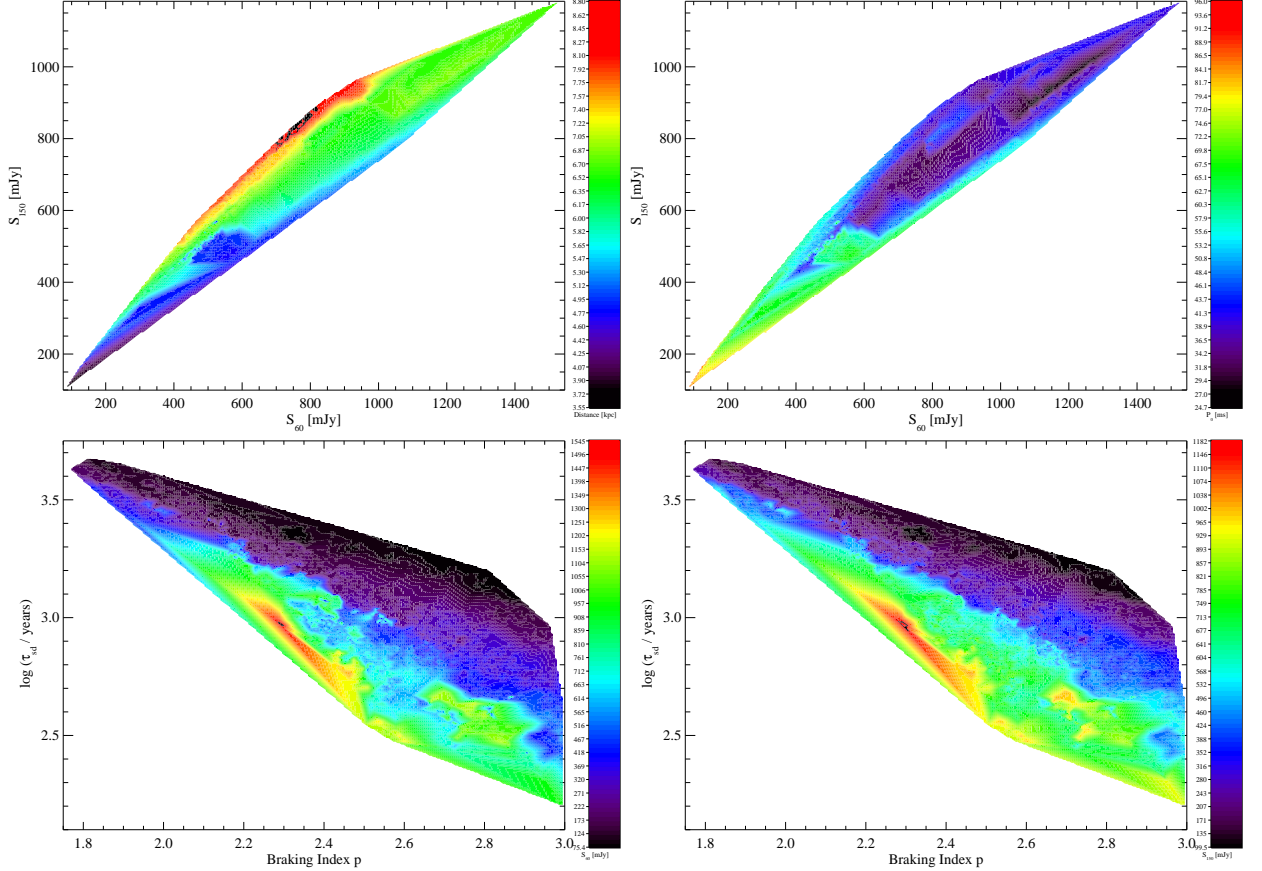


Fig. 19.— *Top:* Distance to (*left*) and initial spin period  $P_0$  of PSR J1930+1852 for predicted values of the 60 MHz  $S_{60}$  and 150 MHz  $S_{150}$  flux densities. *Bottom:* The predicted values of  $S_{60}$  (*left*) and 150 MHz  $S_{150}$  (*right*) flux densities for the braking index  $p$  and spin-down timescale  $\tau_{\text{sd}}$  of PSR J1930+1852. In all cases, only results for MCMC trials with  $\chi^2 < 7.09$ ,  $M_{\text{ej}} < 20 M_\odot$ , and  $p < 3$ . The color bar indicates the  $\chi^2$  of the trial, with red indicating a lower  $\chi^2$  and better fit.

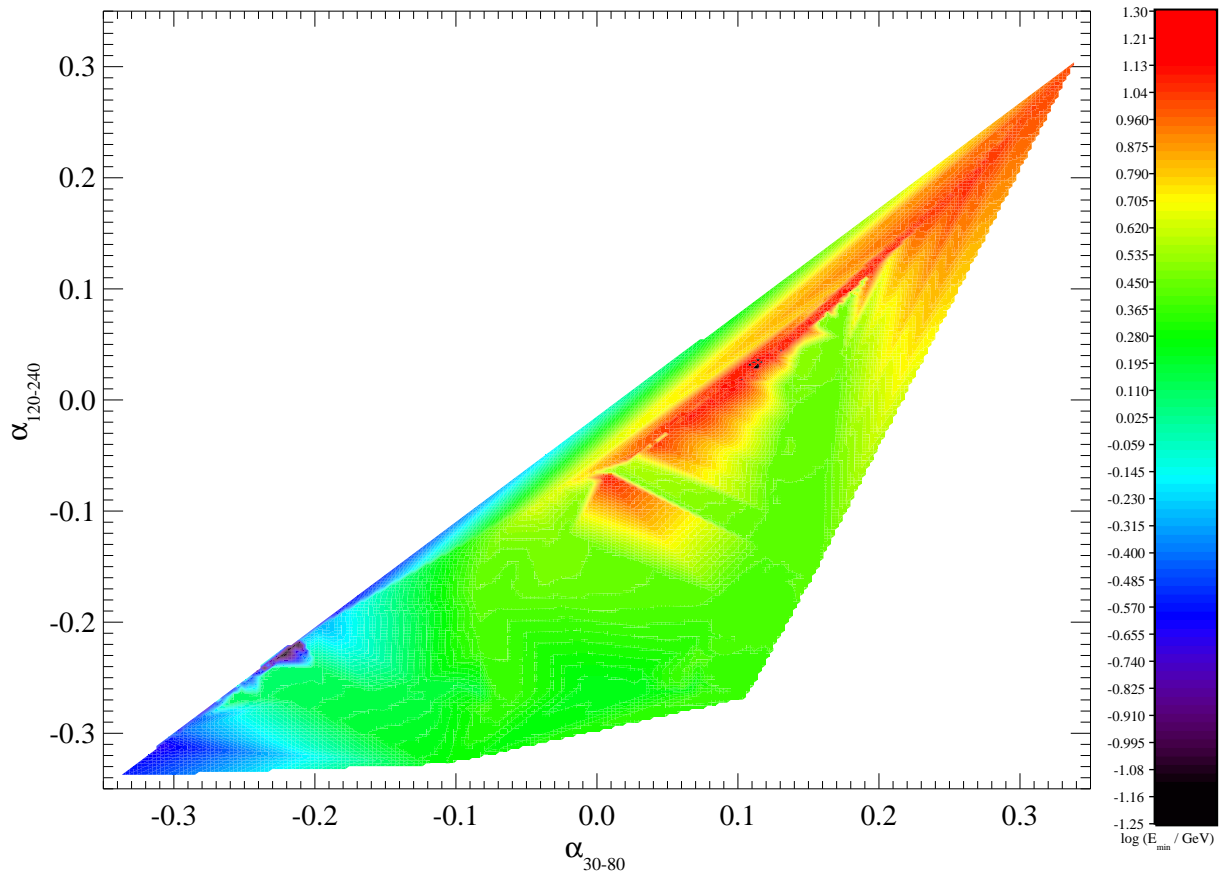


Fig. 20.— Predicted 30–80 MHz ( $\alpha_{30-80}$ ) and 120–240 MHz ( $\alpha_{120-240}$ ) spectral indices of G54.1+0.3 as a function of minimum energy of particles injected at the termination shock ( $E_{\min}$ ) for MCMC trials with  $\chi^2 < 7.09$ ,  $M_{\text{ej}} < 20 M_{\odot}$ , and  $p < 3$ .

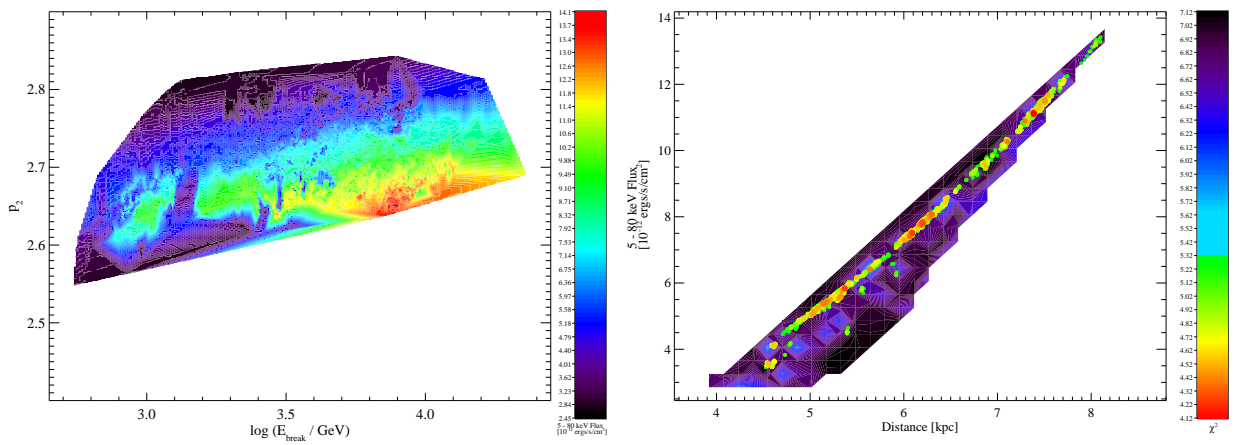


Fig. 21.— The predicted 5–80 keV flux as a function of break energy  $E_{\text{break}}$  and high-energy  $p_2$  index of particles injected at the termination shock (*left*) and the distance (*right*) for MCMC trials with  $\chi^2 < 7.09$ ,  $M_{\text{ej}} < 20 M_\odot$ , and  $p < 3$ . The color bar indicates the  $\chi^2$  of the trial, with red indicating a lower  $\chi^2$  and better fit.

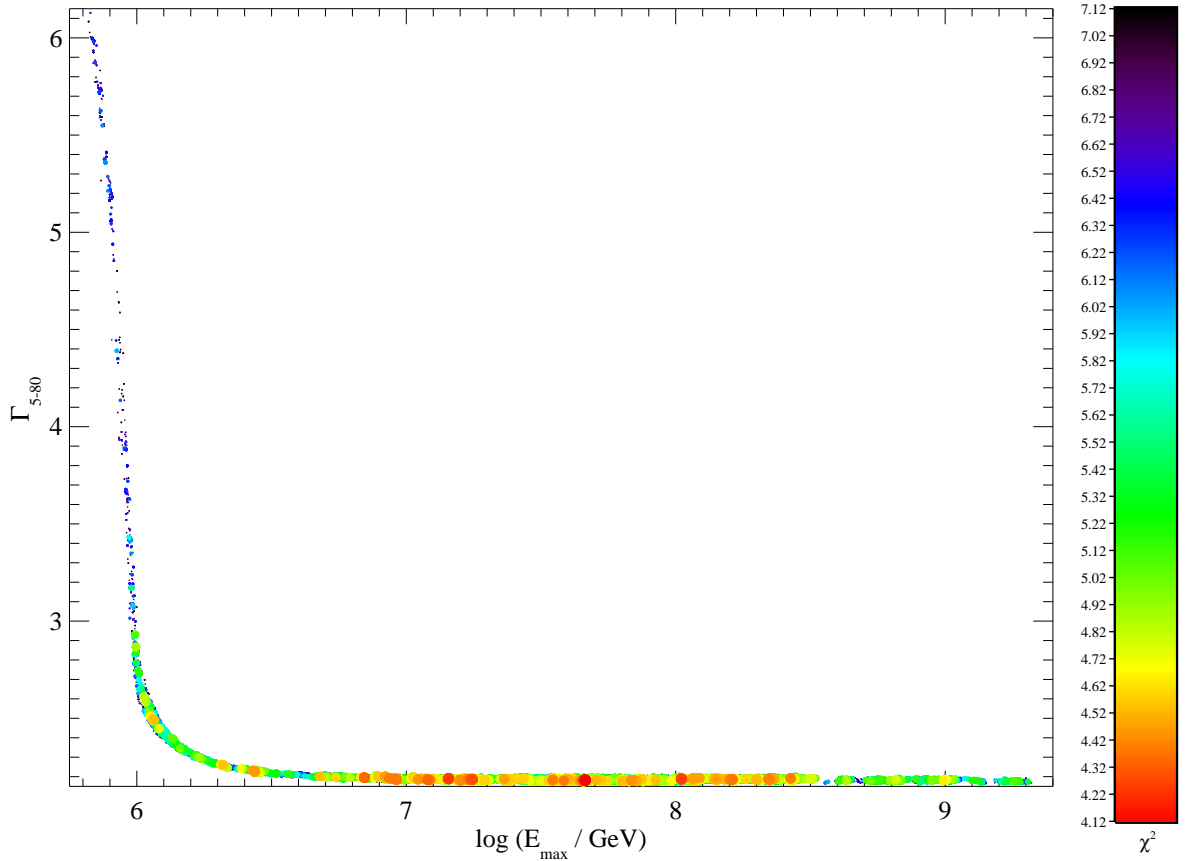


Fig. 22.— The predicted 5–80 keV photon index  $\Gamma_{5-80}$  as a function of the maximum energy  $E_{\text{max}}$  of particles injected at the termination shock for MCMC trials with  $\chi^2 < 7.09$ ,  $M_{\text{ej}} < 20 M_\odot$ , and  $p < 3$ . The color bar indicates the  $\chi^2$  of the trial, with red indicating a lower  $\chi^2$  and better fit.

## REFERENCES

- Acciari, V. A., Aliu, E., Arlen, T. et al. 2010, *ApJ*, 719, L69
- Andrievsky, S. M., Bersier, D., Kovtyukh, V. V., et al. 2002a, *A&A*, 384, 140
- Andrievsky, S. M., Kovtyukh, V. V., Luck, R. E., et al. 2002b, *A&A*, 381, 32
- Arons, J. 2002, in Astronomical Society of the Pacific Conference Series, Vol. 271, Neutron Stars in Supernova Remnants, ed. P. O. Slane & B. M. Gaensler, 71–80
- Blondin, J. M. & Mezzacappa, A. 2007, *Nature*, 445, 58
- Bocchino, F., Bandiera, R., & Gelfand, J. 2010, *A&A*, 520, A71+
- Bogovalov, S. V. 1999, *A&A*, 349, 1017
- Bucciantini, N., Arons, J., & Amato, E. 2011, *MNRAS*, 410, 381
- Bucciantini, N., Bandiera, R., Blondin, J. M., et al. 2004, *A&A*, 422, 609
- Camilo, F., Lorimer, D. R., Bhat, N. D. R., et al. 2002, *ApJ*, 574, L71
- Chen, Y., Zhou, P., & Chu, Y.-H. 2013, *ApJ*, 769, L16
- Chevalier, R. A. 2005, *ApJ*, 619, 839
- de Jager, O. C. 2007, *ApJ*, 658, 1177
- Endeve, E., Cardall, C. Y., Budiardja, R. D., et al. 2010, *ApJ*, 713, 1219
- Fang, J. & Zhang, L. 2010, *A&A*, 515, A20+
- Gaensler, B. M. & Slane, P. O. 2006, *ARA&A*, 44, 17
- Gelfand, J. D., Gaensler, B. M., Slane, P. O., et al. 2007, *ApJ*, 663, 468

- Gelfand, J. D., Slane, P. O., & Temim, T. 2014, Astronomische Nachrichten, 335, 318
- Gelfand, J. D., Slane, P. O., & Zhang, W. 2009, ApJ, 703, 2051
- Ghavamian, P., Laming, J. M., & Rakowski, C. E. 2007, ApJ, 654, L69
- Goldreich, P. & Julian, W. H. 1969, ApJ, 157, 869
- Harrison, F. A., Craig, W. W., Christensen, F. E., et al. 2013, ApJ, 770, 103
- Heger, A., Fryer, C. L., Woosley, S. E., et al. 2003, ApJ, 591, 288
- Ho, W. C. G. & Andersson, N. 2012, Nature Physics, 8, 787
- Kang, H. & Jones, T. W. 2005, ApJ, 620, 44
- Kennel, C. F. & Coroniti, F. V. 1984a, ApJ, 283, 694
- . 1984b, ApJ, 283, 710
- Kirk, J. G. & Skjæraasen, O. 2003, ApJ, 591, 366
- Koo, B.-C., McKee, C. F., Lee, J.-J., et al. 2008, ApJ, 673, L147
- Kozasa, T., Nozawa, T., Tominaga, N., et al. 2009, in Astronomical Society of the Pacific Conference Series, Vol. 414, Cosmic Dust - Near and Far, ed. T. Henning, E. Grün, & J. Steinacker, 43
- Lang, C. C., Wang, Q. D., Lu, F., et al. 2010, ApJ, 709, 1125
- Leahy, D. A., Tian, W., & Wang, Q. D. 2008, AJ, 136, 1477
- Li, H., Chen, Y., & Zhang, L. 2010, MNRAS, 408, L80
- Livingstone, M. A. 2011, PhD thesis, McGill University (Canada)

- Lu, F., Wang, Q. D., Gotthelf, E. V., et al. 2007, ApJ, 663, 315
- Lu, F. J., Aschenbach, B., & Song, L. M. 2001, A&A, 370, 570
- Lu, F. J., Wang, Q. D., Aschenbach, B., et al. 2002, ApJ, 568, L49
- Martin, J., Torres, D. F., & Rea, N. 2012, ArXiv e-prints
- Olmi, B., Del Zanna, L., Amato, E., et al. 2014, MNRAS, 438, 1518
- Ott, C. D., Burrows, A., Thompson, T. A., et al. 2006, ApJS, 164, 130
- Porth, O., Komissarov, S. S., & Keppens, R. 2013, MNRAS, 431, L48
- . 2014, MNRAS, 438, 278
- Reynolds, S. P. & Chevalier, R. A. 1984, ApJ, 278, 630
- Sironi, L. & Spitkovsky, A. 2011, ApJ, 741, 39
- . 2014, ApJ, 783, L21
- Sironi, L., Spitkovsky, A., & Arons, J. 2013, ApJ, 771, 54
- Spitkovsky, A. 2008, ApJ, 682, L5
- Tanaka, S. J. & Takahara, F. 2010, ApJ, 715, 1248
- . 2011, ApJ, 741, 40
- Temim, T., Slane, P., Reynolds, S. P., et al. 2010, ApJ, 710, 309
- Torres, D. F., Cillis, A., Martín, J., et al. 2014, Journal of High Energy Astrophysics, 1, 31
- van Haarlem, M. P., Wise, M. W., Gunst, A. W., et al. 2013, A&A, 556, A2
- Volpi, D., Del Zanna, L., Amato, E., et al. 2008, A&A, 485, 337

Watts, A. L. & Andersson, N. 2002, MNRAS, 333, 943

Woosley, S. E., Heger, A., & Weaver, T. A. 2002, Rev. Mod. Phys., 74, 1015

Zwicky, F. 1938, ApJ, 88, 522